PFC/RR-83-31 DOE/ET/51013-101

A COMPARISON BETWEEN THE RADIAL DENSITY BUILDUP IN THE TARA PLUGS USING HYDROGEN VERSUS DEUTERIUM NEUTRAL BEAMS

Donald T. Blackfield

Plasma Fusion Center
Massachusetts Institute of Technology
Cambridge, MA 02139

November 1983

This work was supported by the U. S. Department of Energy Contract No. DE-AC02-78ET51013. Reproduction, translation, publication, use and disposal, in whole or in part by or for the United States government is permitted.

ABSTRACT

The WOLF code is used to compare the beam divergences from a TARA source using hydrogen and deuterium. Factors which influence the divergence which are investigated are the electron temperature, initial ion energy, electrode positions and ion beam current density. The beam divergence for 20 keV hydrogen is found to be only 20% smaller than for 25 keV deuterium for the same electrode positions. Since the optimal positioning of the electrodes is found to be independent of mesh spacing, a large parameter study is undertaken using little computer time.

A time-dependent radial Fokker-Planck code is next used to examine the radial density buildup in a plug of the TARA tandem mirror. For both hydrogen and deuterium neutral beams, the influences of beam positioning, current and energy, edge neutral pressure and assumed electron temperature are studied. In TARA, hydrogen beams produce a higher density with a narrower profile. In both hydrogen and deuterium, shifting the beam 3 cm above the midplane produces the "optimal" density profile. Buildup is achieved for edge pressures less than 1 x 10 -> Torr. Finally, higher electron temperatures can cause a lower density buildup due to greater electron endlosses, decrease in the electron impact ionization cross section and increase in the ion loss cone.

INTRODUCTION

The Livermore tandem mirror experiment TMX has obtained a sloshing ion distribution when deuterium neutral beams were injected into the plug region after being unsuccessful with hydrogen neutral beams. This has motivated the design group of TARA to consider changing from a hydrogen experiment to deuterium. For the neutral beam group this would mean changing from 20 keV hydrogen to injecting 25 keV deuterium into the plugs. Several physics issues must be addressed in order to consider the overall effect on plasma performance if this change is made. Several fundamental plasma parameters are functions of ion mass and velocity. In TABLE 1 some of these parameters are shown for 20 keV hydrogen and deuterium and 25 keV deuterium slowing down on a background plasma with ion energy of 10 keV and electron energy of 150 eV with a density of 2×10^{12} cm^{-3}. For example with deuterium the charge to mass ratio is larger. Using Spitzer's formula for the 90 degree scattering time [1],

$$t_{90^o} = \frac{m^{1/2}(3kT)^{3/2}}{8 \times 0.714\pi ne^4 \ln\Omega} \tag{1}$$

confinement should be better. However the slowing down time for 25 keV deuterons on a deuterium plasma is also longer [1-2],

$$t_s = \frac{3\pi^{1/2}}{2(1 + m/m_f)A_D l_f^3} \tag{2}$$

with

$$A_D = \frac{8\pi e^4 n_f \ln\Omega}{m^2} \tag{3}$$

and

$$1_f^2 = \frac{m_f}{mkT_f} \tag{4}$$

so less neutral beam energy may be deposited in the plugs. The deuterium higher mass and energy results in an increase in electron drag while pitch angle scattering is decreased. The Larmor radius for deuterium is larger than for hydrogen so less Larmor radii "fit" within the plasma. Finite Larmor Radius (FLR) effects are increased and radial profiles become more important.

Several physics issues may be raised when deuterium neutral beams are used. Is the amount of cold streaming gas affected? Should one build up to a higher or lower density with deuterium? Should the larger Larmor radius cause a shift in the injection angle to obtain the desired density? What is the effect on the plasma halo with deuterium? Since the ion gyrofrequency decreases for deuterium either the rf generating frequency needs to be decreased or higher harmonic heating will occur. If the magnetic field is doubled to heat at the fundamental resonance, how is the plasma affected?

The above are all important considerations which need to be examined. Since changing from hydrogen to deuterium may have a large impact on the TARA design we have decided to examine this problem in four steps. The first step is to examine the effect of changing from 20 keV hydrogen to 25 keV deuterium on the neutral beam source design. The results which will be summarized below were obtained from the WOLF code [3-4]. It appears that the source does not need to be redesigned although the beam divergence increases slightly.

The next step is to examine the effect of the higher energy deuterium neutral beams on the buildup of the confining plugs in TARA. This is examined using a time-depenedent Fokker-Planck buildup code which uses a square-well approximation for the spatial variation of the ambipolar potential and magnetic field [5]. This code uses finite width neutral beams with three energy components to examine the time evolution of the plasma density and temperature profiles but assumes uniformity in the axial dimension . The preliminary results show that the plasma does not build up to as high a central density with 25 keV deuterium beams although the plasma is broader.

However it is shown that TARA should have enough neutral beam current to build to a reasonable density.

Next, a multi-cell, multi-species, time-dependent 0-D particle and energy balance code is being developed to examine the TARA design [6]. This code will be used to examine the impact of changing from hydrogen to deuterium using existing theories. Finally the effects of deuterium on the various proposed ICRF schemes will be examined using both an existing slab model code [7] and a 0-D time- dependent Fokker-Planck code [8-9]. In addition a bounce-averaged Fokker-Planck code [10] has been developed that, with modifcations, can be used to further understand the effects of ICRF in TARA. The above questions and methods involve a long-range study. In this paper both WOLF and buildup results will be presented.

WOLF RESULTS

The WOLF Code, a set of programs which calculates ion trajectories in two dimensions through a set of electrodes, attempts to minimize the beam divergence and obtain a self-consistent shape and position of the emitting surface. Factors which influence the beam divergence which we investigate are the electron temperature, initial ion energy, electrode positions, and the ion beam current density. For a given ion energy and electron temperature, emitter position, ion current density and electrode positions we try to minimize the beam divergence and deform the emitting surface to achieve a predetermined electric field at the emitting surface.

FIGURE 1 shows the electrode positions, equipotential lines and ion trajectories for a 20 keV hydrogen beam calulation. Due to the symmetery of the problem only half the beams are shown. WOLF attempts to deform the emitter surface to obtain an electric field value near 300 V/cm, consistent with the calculations by Self [11]. The greater the electric field at the emitter, the smaller the beam divergence. WOLF attempts to obtain a value of 300 V/cm for each mesh interval. For this "optimized" case the rms beam divergence is 0.0236 radians and the rms deviation in the electric fields from 300 V/cm is 291.6 V/cm.

FIGURE 2 shows the geometry of the emitting surface for the 20 keV hydrogen and the 25 keV deuterium cases. The points marked by the squares show the emitter position for both these cases. The diamond points show the emitting surface for a nearly optimized 25 keV deuterium case. Later we will examine the sensitivity of our results to the assumed emitting surface.

For the same geometry as the 20 keV hydrogen case, the rms beam divergence is 0.0277 radians with an electric field rms deviation of only 60.1 V/cm. FIGURE 3 shows the geometry and ion trajectories for this 25 keV deuterium case.

FIGURE 4 shows the sensitivity of beam divergence to the assumed electron temperature. Again the diamond shaped and the square shaped points correspond with the two surfaces in FIGURE 2. As the electron temperature increases, the electric field at the surface of the emitter increases while the beam divergence decreases. FIGURE 5 shows how the rms beam divergence varies with initial ion temperature. The ions initially are assumed to be maxwellian, drifting with the electron temperature [3].

FIGURES 6 and 7 show the sensitivity of beam divergence and rms electric field deviation with beam current. If only FIGURE 6 was examined one might draw the conclusion that a lower beam current than the highest achievable value of 0.390 A/cm^2 [12] might be better. However, FIGURE 7 shows that the calculated electric fields are larger than the desired value of 300 V/cm when the current density decreases. To obtain a value of 300 V/cm the plasma surface must be moved away from the extractor electrode and the beam divergence would then increase. On the other hand, for the larger values of current density, the calculated electric field values are too small. Therefore, if the emitter surface is moved closer to the extractor to increase the electric field, the beam divergence would again increase.

FIGURE 8 shows how the beam divergence varies with distance between the emitter surface and the acel electrode. At points A, B, and C the emitting surface had to be moved so that the code could converge to a solution. In general for a given optimized solution the beam divergence will quickly

increase as the electrode positions are moved relative to the emitting surface. The distance between the acel and decel electrodes has a much smaller effect on the beam divergence.

Finally we have investigated the sensitivity of our results to the "coarseness" of the mesh, hence the number of individual beamlets which we use in calculating the beam divergence. FIGURE 9 shows a typical triangular grid used in the coarse mesh calculations which have been presented. A typical "fine" mesh grid is also shown in FIGURE 9. A fine mesh 20 keV hydrogen ion trajectory and equipotential line plot is shown in FIGURE 10. Five times more beamlets are used to obtain a more accurate solution. A comparison of 20 keV hydrogen beam divergences for various current densities can be seen in FIGURE 11. Although the beam divergence decreases with the finer mesh, the optimal current density remains the same. Therefore a coarse mesh, which requires a smaller amount of computer usage, can be used in a parameter study to obtain an optimal design.

In conclusion we have found that when 25 keV deuterium beams are used instead of 20 keV hydrogen beams, the neutral beam ion source does not need to be redesigned, assuming an increase, perhaps as large as 20%, in beam divergence is acceptable. The maximum extractable beam current should be similar since the space-charge current limitation [13],

$$J = \frac{1}{9\pi}\left(\frac{2e}{m}\right)^{1/2}\frac{V^{3/4}}{d^2} \qquad (5)$$

is the same for both cases. Assuming that 25keV deuterium beams can be successfully injected into the plugs of TARA we next examine the time-dependent density buildup of the plugs with these beams.

BUILDUP RESULTS

A time-dependent, multi-species, Fokker-Planck code has been developed by Futch and others [5] to calculate f(r,v,t) using an orbit-averaged treatment of Coulomb collisions and includes the finite Larmor radius of the ions. This model calculates the ion distribution function in the plug region in one dimension in velocity space (v), and in the radial dimension in real space (assuming cylindrical geometery). A perpendicular injected finite width neutral beam is assumed to be incident a distance d above or below the magnetic axis. The beam is assumed to be gaussian-shaped in the radial direction and expotentially decaying axially. Since the neutral beams in TARA will be injected at 30-40 degrees it is difficult to determine the actual beam requirements from only a radial treatment. Defining cb1 and cb2 to be the equivalent distances above and below the magnetic axis for a uniform neutral beam injected perpendicular ($\theta = 90°$) and assuming that the beam is gaussian in the z-direction

$$J(z) = J_0 e^{-z^2/13^2} \tag{6}$$

the total beam current would be

$$I_{total} = \sum_{i=1}^{3} J_i \quad [cb1 + cb2]L_z \tag{7}$$

$$= 1.602 \times 10^{-19}[1.372 \times 10^{18}][1 + 2/3 + 1][10] \int_{-13}^{13} e^{-z^2/10^2} dz$$

$$= 113A$$

where cb1=1.5Xcbm1 and cb2=1.5Xcbm2 and cbm1 and cbm2 are the 1/e points above and below the magnetic axis for the neutral beam footprint. However, since the beam is injected at 40 degrees, the axial extent is increased so the effective beam current needed is decreased by sin(θ)

$$I_{total} = 113 \times \sin(\theta_{inj}) = 113 \times \sin(40^{o}) = 73A \qquad (8)$$

Since the beam particles once they are ionized bounce along z between the mirror points, the effective beam density decreases so a larger beam current is required. In addition the actual gaussian shape of the beam in the z-direction may be larger than EQUATION 6 shows. If we include a factor to account for these effects we may write EQUATION 8 as

$$I_{total} = C(\text{r profile, z profile, z bounce pt.}) \times 113 \times \sin(\theta_{inj}) \qquad (9)$$

$$\approx 100A$$

We have decided to pick C so that the total current is 100 Amps. The buildup code only uses J_1, J_2, J_3 so that even though the absolute value of the beam current cannot be calculated the scaling with beam current can be (for the same injection angle) determined.

In addition to neutral beams, the model also takes into account the presence of Franck-Condon neutrals at the plasma edge. Assuming that these neutrals comprise 10% of the total cold gas at the plasma edge [14] the edge pressure is given by

$$P = \frac{\text{fcnum}}{3.2 \times 10^{15}} \text{ Torr} \qquad (10)$$

where fcnum is an input.

This model has been modified to take into account the time-dependent influx of cold gas due to the neutral beam injection. The following expression approximates the assumed neutral gas rise at the plasma edge [6]

$$n_{fc} = \text{fcnum}(1 - e^{-4t} + .001) \qquad t < 5\text{ms} \qquad (11)$$

and is plotted in FIGURE 12.

The initial plasma parameters are given in TABLE 2. We first compare the buildup of a TARA plug cell using the two base cases; 20 keV hydrogen beams and 25 keV deuterium beams. Both cases assume 100 Amps on target and that the edge pressure initially is 10^{-8} Torr (fcnum in Eq. [10] equals 3.2×10^{10}). In all cases anomalous electron heating (ECRH) or energy transport was assumed to keep the electron energy fixed. For most cases, E_e=100 eV, although we also examined E_e= 250eV, 500eV, 750eV and 1000eV. Fixing E_e often resulted in the code stopping when the ambipolar potential requirements could not be satisfied after a set number of iterations (200). In the other cases, the simulations were for 400 time steps when t=10.0 ms. With a time varying edge pressure, no cases reached equilibrium. However by 4 ms (200 time steps) our base cases had sufficient density buildup and run longer than the global cofinement time of 2 ms. To determine how the density buildup varies with species, neutral pressure, E_e, and beam parameters, we will examine all cases at the same point in time, t= 4ms (200 time steps) which is earlier than the occurrence of any ambipolar potential problems and is larger than the global confinement time.

FIGURES 13-14 show that the initial ion density and energy profiles are slightly different. In all cases, the same number of velocity and spatial mesh points are used. Since deuterium has a greater mass, both the velocity and spatial points are further apart. This introduces a slighlty larger numerical inaccuracy when calculating densities and energies at a given radial point. For hydrogen, the peak density is 1.8×10^{12} cm^{-3} with an average density of 6.0×10^{11} cm^{-3} while the peak deuterium density is 1.4×10^{12} cm^{-3} with average density of 4.4×10^{11} cm^{-3}. In both cases this is lower than the inputed starting peak value of 2.0×10^{12} cm^{-3}. We have assumed that the initial distribution is gaussian shaped. However an ion distribution in the plug cannot be gaussian in the presence of a loss cone. The code assumes that all particles in the loss cone are instantaneously lost from the system. Therefore the overall density is decreased because particles

are "deposited" into the loss cone. In addition, there is an initial radial dependence

$$n(1)\alpha(1 - r^2/r_{pi}^2(v)) \tag{12}$$

$r_{pi}(v)$ is the radial point where $r_{pi} + \rho_{\perp i}(v) = r_p = 14.75$ cm. Therefore r_{pi} is the plasma radius and is a function of velocity. Any particle whose perpendicular velocity results in a Larmor radius excursion beyond the maximum radial grid point is lost thereby decreasing the actual plasma radius for this velocity at this radial point. Since deuterons have a larger larmor radius than protons, their initial density is smaller.

FIGURES 15-16 show the time evolution of the ion density for the two base cases (see TABLE 3). Although the hydrogen case starts with a slighlty higher initial density, at 4 ms, the average density is 5.4×10^{12} cm^{-3} while the deuterium density is only 2.2×10^{12} cm^{-3}. However, the larger deuterium Larmor radius causes the density profile to be broader; the radius at which the electron density equals 1.0×10^{-4} times the peak density is 14.7 cm for deuterium and is 14.0 cm for hydrogen. The hydrogen global particle confinement time is also larger, 2.2 ms as compared to 1.7 ms for deuterium. The dominant system power losses in both cases are electron and ion end losses and charge exchange from the Franck-Condon neutrals. For hydrogen, these values are 9.0 kW, 23.5 kW and 4.8 kW while for deuterium, they are 7.4 kW, 2.1 kW and 3.0 kW. The electron endloss is the pastukov loss and is defined as [13]

$$(n\tau)^{-1} = \frac{2}{\pi^{1/2}} \frac{n_e}{\tau_s} \frac{2R}{2R+1} \frac{\exp\left(-\frac{e\phi}{T_e}\right)}{\ln(4R+2)} \frac{T_e}{e\phi} \left[1 + \frac{T_c}{2e\phi} - \frac{1}{4}\frac{T_e}{e\phi} + \ldots\right] \tag{13}$$

The ion endloss is determined from the loss of particles to the loss cone. In all cases the ions are assumed to initially have a uniform temperature profile with an energy of 10 keV. An energy source is the ionization of the neutral beam by ion and electron impact and the charge

exchange of neutral beam atoms with energies larger than 10 keV. Charge exchange with atoms below 10 keV causes a loss of energy. The trapping power is the sum of the charge exchange and ion and electron ionizations. For the two base cases the total trapping power for hydrogen is 143 kW with 13 kW of net power coming from charge exchange. For the deuterium case only 32 kW of beam power is trapped with 2.2 kW coming from charge exchange. Some of the increase in trapping power is due to the higher initial density in the hydrogen case. In the APPENDIX the cross sections and σv's for charge exchange and ion and electron ionizations are shown. Although the σv for the trapping of 25 keV deuterium neutral beams is nearly the same as for 20 keV hydrogen the lower energy components of the 20 keV hydrogen beam have a higher trapping σv than the half and third energy components of deuterium. Consequently more of the hydrogen neutral beam is trapped which leads to a higher density which in turns leads to a higher trapping rate. At these low energies, charge exchange is the largest contributor to the trapping cross section. FIGURE A-1 in the APPENDIX shows that the hydrogen charge exchange cross section is larger. The ion impact ionization for hydrogen is smaller. The electron impact ionization cross section is also small and is the same for both species. This cross section depends only upon the electron temperature since the electrons are assumed to travel much faster than the neutral beam atoms. Finally, the vessel walls are considered far enough removed from the plasma so that wall losses (~1 W) can be ignored.

FIGURES 15-16 also show the time evolution of the ion energy profiles. In both cases ion heating (ICRF) was assumed to be present so that the initial ion energy was 10 keV (T_i=6.7 keV) which is close to the ion energy at 4.0 ms. In the hydrogen case, the peak energy at the edge is almost 21 keV, which is higher than the neutral beam energy. However, at this point, the ion density is less than 6.0×10^8 cm^{-3} at r=13.75 cm. This somewhat high value may not be physical (up scattering or interaction with the radial potential profile) but could be numerically produced. Although the density may still continue to rise, FIGURES 15-16 show that the ion temperature profile quickly reaches a steady-state. The electron energy is held constant at 100 eV so there is a large flow of energy from the ions to the electrons.

Finally FIGURE 17 shows the time evolution of the log of the density profile of the Franck-Condon neutrals for both cases. As the central density rises, the hydrogen Franck-Condon neutrals are expelled from the center. Their density rises at the edge due to the assumed increase in edge pressure with time. At t=0 ms, there is assumed to be no Franck-Condon neutrals in the plasma. In the deuterium case, the central density is not high enough to significantly expel the Franck-Condon neutrals. There is less than an order of magnitude decrease in neutral density from the edge to the center. Although there is more neutral gas charge exchange power loss in the hydrogen gas case (since there is more system energy) the actual amount of charge exchange power loss from the center is approximately three times smaller than the deuterium case.

In the hydrogen case, with 100 Amps of 20 keV of neutral beams, the average density increases from 6.0×10^{11} cm^{-3} to 1.1×10^{13} cm^{-3} in 4 ms with a peak value near 2.2×10^{13} cm^{-3} while for deuterium, n_e average increases from 4.0×10^{11} cm^{-3} to 2.2×10^{12} cm^{-3} with a peak near 6.2×10^{12} cm^{-3}. In both cases there is a sufficient buildup of density in 4 ms. The buildup code is optimistic since it has only radial variations. However, TARA should have over 150 Amps of beams so there is a rather wide margin to allow for buildup. Having examined in detail our two base cases, we now proceed to examine how the density varies when neutral beam position, energy, current, neutral edge pressure and the fixed electron temperature are varied.

DENSITY BUILDUP AND BEAM POSITION

FIGURES 18-20 show the hydrogen ion density, energy and Franck-Condon profiles at t=4.0 ms for several values of d from -3 cm to 10.5 cm. As d increases, the peak ion density increases. The ion energy remains fairly constant except for d= 10.5 cm. As FIGURE 20 shows, the Franck-Condon neutral density at the center becomes appreciable for $d \leq 1$ cm. For these values of d, there is little density buildup. The average electron density versus d is plotted for these cases in FIGURE 21. We see that the average density increases with d until d gets too large. When a charge exchange or

ionization event occurs, the finite Larmor radius of the beam shifts the particle guiding center towards the minus d-direction. Therefore, by shifting the beam above the axis, more beam particles are trapped. However, if the beam is shifted too far above the axis, the radial decrease in density produces a decrease in beam trapping (shown in FIGURE 22). In addition, the profile becomes very peaked. Besides peaking the density and generally increasing n_e, the plasma radius shrinks from 14.8 cm to 13.0 cm as d increases. The beam charge exchange power increases with d from 0 kW to 50 kW until d gets too large when it drops to 10 kW. The higher average and peaked density causes more of the beam to be trapped. The shrinking plasma radius and peaking density has little effect on the density-squared weighted global confinement time defined as

$$\langle \tau_p \rangle \equiv \frac{\int n_e^2 d^3v}{\langle n_e \rangle \int \frac{\Delta n}{\Delta t} d^3v} \qquad (14)$$

and

$$\langle n_e \rangle = \frac{\int n_e d^3v}{\int d^3v}$$

which is between 1.8-2.5 ms. The increase in density is also followed by increases in both the ion and electron endloss terms and charge exchange with the neutral gas, shown in FIGURE 23.

When 25 keV deuterium beams are used, the behavior of the density buildup with beam position is slightly different. The density profile is broader and the plasma radius is less sensitive to beam position. The plasma radius is 14.7 cm which is larger than for hydrogen. The larger Larmor radius tends to "smear" out the effect of moving the finite width beam. As FIGURES 24-25 show, as d increases, the average density and peak density again increase. However, the larger Larmor radius causes a peaking of the density off axis as d increases. For $d \leq -3$ cm, there is little density buildup. FIGURE 26 shows that for $d \leq 1$ cm the ion energy is lower than the initial 10

keV. For d=10.5 cm, there is significant beam trapping (60 kW) so that the ion energy is significantly higher near the edge. FIGURE 27 shows that there is sufficient density for $d \geq 1$ cm to prevent a large fraction of Franck-Condon neutrals from penetrating to the center. Except for the highest buildup case (d=10.5 cm) there is little change in either the electron or the ion endlosses. The higher ion temperature and density for d=10.5 cm results in more electron (18 kw) and ion (4.5 kW) endloss power. As d increases, the Franck-Condon neutrals in the plasma density decreases and this results in a smaller fraction of the total energy loss through charge exchange on the cold gas (shown in FIGURE 28). As d increases from -0.5 cm to 10.5 cm, the average n_e increases 7 times while the charge exchange of the gas increases only 4 times. In addition, we again see in FIGURE 29 the trapping power increasing with density, hence d . The global particle confinement time remains from 1.6-1.8 ms except for the higher density, d=10.5 cm, case where the off axis peaking in density results in a $\tau_p = 0.45$ ms. Although the beam trapping power increases from 0.5 kW to 6 kW as d increases from -5 cm to 5 cm, for d=10.5 cm, there is a sharp drop in the charge exchange power from the beam to 0.4 kW. Because the ion energy is close to 20 keV near the edge where the beam is trapped, the full energy component does not add much energy to the plasma while charge exchange with the half and third energy components causes a decrease in plasma energy. The dominant power contribution is from ionization of the beam which increases with both density and ion temperature.

For both hydrogen and deuterium, a neutral beam of width 7 cm displaced 3 cm above the midplane provides a sufficient density buildup within 4 ms and density peaked on the midplane with a relatively small density gradient. Consequently, on changing from 20 keV hydrogen to 25 keV deuterium, the neutral beamline does not need to be repositioned, provided that a slightly broader (14.75 cm as compared with a 14.2 cm) but lower density (2.2×10^{12} cm^{-3} as compared with a 5.8×10^{12} cm^{-3}) plasma is tolerable.

BUILDUP VERSUS NEUTRAL BEAM CURRENT

We next examined the scaling of the TARA plasma buildup with beam current fixing the hydrogen full energy component at 20 keV and the deuterium at 25 keV. The ratio of full to half to third energy component beam densities remains 1:2/3:1. This corresponds to a beam energy mix at the source of 60% full energy, 20% half energy and 20% third energy. The $H_2(D_2)$ half energy molecules split into two H(D) ions while the third energy $H_3(D_3)$ molecules split into three H(D) ions. We investigate buildup for incident beam currents of 50A, 75A, 100A (base case), 125A and 150A. FIGURES 30-31 show that the density buildup is proportional to beam density. However, this increase is nonlinear since the the beam current varies from 50-150 A while the average density changes from 1.9×10^{12} cm^{-3} to 23.1×10^{12} cm^{-3}.

The nonlinear behavior in the density buildup is also shown in the total beam trapping power plotted in FIGURE 32. The amount of power to the plasma from charge exchange of the beam is similar rising from near 0 kW at 50A to almost half (259 kW out of 566 kW) at 150A. The ion temperature profiles do not change significantly with beam current while FIGURES 33-34 show that with the rising density, the amount of neutral gas, hence the amount of power lost to charge exchange increases at a smaller rate (2.4 kW up to 5.1 kW) than the increased energy content in the plasma. The global particle confinement time, decreases as the density increases (FIGURE 35), since there are more particle interactions. However $n\tau_p$ increases with increasing current. As the current increases from 100A to 150A the plasma radius decreases from 14.45 cm to 12.8 cm. The higher peak density causes the $1.0 \times 10^{-4} \times n_o$ point to shift inwards.

Similar results are obtained for 25 keV deuterium. FIGURES 36-37 show the density profile and average density for deuterium. There is again a nonlinear increase in average density (from $0.8 \times 10^{12} cm^{-3}$ for 50 A to $8.0 \times 10^{12} cm^{-3}$ for 150 A) however the plasma radius again remains constant at 14.7 cm. In all cases the large Larmor radius creates a broader plasma with a

slight density peak off the midplane (near the injection point r= 3 cm). The ion temperature profile is again unchanged with beam current remaining near 10 keV with a slight dip at the center and peaking up to 15 keV near the edge. FIGURES 38-39 show a similar behavior for the franck-condon neutral penetration and the resultant charge exchange power loss. The charge exchange power loss varies linearly with beam current rising from 1.4 kW at 50 A to 4.9 kW for 150 A of beam current. FIGURE 40 shows the increase of beam trapping power with beam current. The fraction of charge exchange power which contributes to the total trapping power of the beam is lower than for hydrogen, being from 5-10% as compared to 10-45% for the higher current hydrogen cases. The ion ionization σv is higher at higher energies while the charge exchange σv for deuterium tends to trap a higher ratio of low energy components to full energy ions. In additon the larger Larmor radius causes a greater fraction of the full energy ions to leave the plasma. The broader plasma profile also causes a higher percentage of the charge exchange events to occur near the plasma edge. Again although the global confinement time decreases from 3.3 ms to 1.1 ms, $n\tau_p$ doubles when the current changes from 50 A to 150 A.

It is obvious from above that increasing the beam current will result in higher densities and increased $n\tau_p$. The increased in density is greater than a linear variation. For deuterium which has a broad profile, the plasma radius does not change. For hydrogen the rise in central density also results in a somewhat smaller radius. The next effect we examine is, on keeping the current constant, how the density buildup scales with beam energy.

BUILDUP VERSUS NEUTRAL BEAM ENERGY

In this section we examine how both hydrogen and deuterium density buildup scales with beam energy. We have kept the total current constant at 100 Amps and have kept the ratio of full to half to third energy components the same while the full energy component varies from 15 keV to 30 keV. FIGURE 41 shows that the peak density varies inversely with beam energy. The lower the beam energy, the more beam trapping occurs. The average density, shown in FIGURE 42 shows a weak dependence with beam energy until the beam energy

approaches 30 keV. At 30 keV, the beam energy is so high that much less trapping occurs and the average density falls. The effect of beam energy on the ion temperature can be seen in FIGURE 43. The higher the beam energy, the higher the ion energy until E= 30keV. The plasma radius is largest (14.7 cm) for small E (15 keV), the case where the most beam is trapped. In this case more beam is trapped further from the center and the plasma is somewhat larger. When the beam energy is raised, the plasma radius shrinks to 14.2 cm for 30 keV neutral beams. The beam trapping power (P $\sim$ 140 kW) remains constant until E= 30 keV, where there is a sharp drop to 40 kW. FIGURE 44 shows that except for E=30 keV there is little difference in the amount of Franck-Condon neutral penetration, the amount of energy being lost to charge exchange with cold neutrals being from 3.6-4.7 kW until E= 30 keV where a higher percentage of total power (1.7 kW) is lost. The global confinement time is relatively insensitive to beam energy being between 2.0 ms to 2.4 ms.

Since deuterium has a larger Larmor radius, the variation in beam energy has a greater influence on the plasma buildup. In addition to the decrease in the trapping rate as the energy is increased, the density shown in FIGURES 45-46 decreases from an average n_e of $6.3 \times 10^{12} cm^{-3}$ for a 15 keV neutral beam to $1.8 \times 10^{12} cm^{-3}$ for a 30 keV beam. The Larmor radius increasing with energy, produces a broader plasma (shown in FIGURE 45). The ion temperature increasing with beam energy is shown in FIGURE 47. The change in beam energy has little effect on the power loss to the cold neutrals (2.8-3.4 kW) although the higher peak density excludes more of the neutrals in the plasma core shown in FIGURE 48. The beam trapping power plotted in FIGURE 49 decreases with increasing energy since the density decreases. The power gained from charge exchange with the deuterium beam falls from 8.7 kW to 1.7 kW as the beam energy varies from 15 keV to 30 keV. Although the charge exchange cross section (see APPENDIX) is larger than the ionization cross sections, the net amount of power gained through charge exchange events is greatly reduced since hot plasma particles are lost in this interaction. The global confinement time remains fairly constant as the density drops,increasing from 1.5 ms to 1.75 ms. However, the actual measure of confinment, $n\tau_p$ decreases as the beam energy increases.

It can be seen that in both the hydrogen and deuterium cases, the lower beam energies produces a higher density but at slightly lower temperatures. To buildup in a shorter time or to a higher density, one should increase the current at the expense of beam energy. The effect of changing the energy has a lesser impact in a hydrogen plasma where the Larmor radius is smaller. However near 30 keV the Larmor radius is large enough to cause a drop in the buildup density. There appears to be little gained by increasing the beam energy from 15 keV to 25 keV and this increase could result in a lower density plasma if the beam current is significantly reduced. The deuterium case shows a monotonic decreasing density as the beam energy is increased. With both species $n\tau_p$ decreases as beam energy increases.

BUILDUP VERSUS NEUTRAL GAS PRESSURE

In this section we examine how the TARA plug density buildup is influenced by the time-dependent neutral gas pressure at the plasma edge (see EQUATION 11). In this study we have varied fcnum from 3.2×10^{8} to 2.0×10^{11} which corresponds to an edge neutral density (see EQUATION 10) at t=0 ms from 1.0×10^{-10} Torr to 6.0×10^{-8} Torr and rising exponentially to 17 times this value at t=4 ms.

FIGURE 50 shows that there is little affect on the hydrogen density buildup as the neutral gas pressure is raised from 1.0×10^{-10} Torr to 3.0×10^{-8} Torr. The central density begins to decrease when the neutral pressure at the edge is initially 6.0×10^{-8} Torr. The franck-condon neutral profiles are shown in FIGURE 51. As the neutral pressure increases, the plasma shrinks from 14.5 cm to 13.7 cm. The beam trapping power remains fairly constant near 145 kW until the higher pressure causes the central density to drop which in turn results in a decrease in trapping power (112 kW). In the highest pressure case the ion temperature is somewhat cooler at 4 ms (shown in FIGURE 52). The global confinement time decreases from 2.4 ms to 1.65 ms resulting in a decrease in $n\tau_p$ over this range of approximately the same ratio. In this range the power lost through charge exchange on the cold gas increases

from 20 kW to 25 kW. For hydogen, we can conclude that an initial edge pressure as high as 6.0×10^{-8} Torr, rising to 1.0×10^{-7} Torr after 4 ms can be tolerated with only a slight decrease in plasma density. Unfortunately, it appears that the deuterium plasma, with its broader and lower density profile is more sensitive to the edge pressure.

FIGURES 52-54 show that both the central and peak density decreases as the edge neutral pressure is increased. At the highest initial edge pressure there is very little buildup, the average n_e increasing from $4.8 \times 10^{11} cm^{-3}$ at t=0 to $8.0 \times 10^{11} cm^{-3}$ at t=4 ms and actually decreases below this value due to the increasing edge pressure for $t \geq 4$ ms. It appears that with our model an edge pressure of 1.0×10^{-6} Torr at t=4 ms is too high to allow the plasma to buildup. In the pressure range we have examined neither the ion temperature nor the plasma radius (14.7 cm) changes. With the decrease in density as the pressure increases, the beam trapping power (see FIGURE 55) decreases from 36 kW to 11 kW while the amount of neutral gas which reaches the center as well as the power lost from the resultant charge exchange increases. Unlike hydrogen, the increased penetration of the edge neutrals causes a significiant decrease in $n\tau_p$ over this pressure range. An initial edge pressure of 6.0×10^{-8} Torr appears to be too high to achieve a density buildup in TARA. If the edge pressure is found to be difficult to control, a likely prospect when neutral beams are used, a better buildup should be achieved with hydrogen. Initial edge pressures greater than 10^{-7} Torr may be too high for either species. In all of the previous cases, we have kept the electron energy fixed at 100 eV. We next vary the electron energy to determine its affect on the density buildup.

BUILDUP VERSUS ELECTRON TEMPERATURE

In this section we examine the buildup of the TARA plug when the electron energy is varied from 100 eV to 1000 eV. FIGURES 56-57 show that for hydrogen, both the peak and average density drops as the electron temperature increases. The ion temperature profile is unchanged but the neutral gas

penetration shown in FIGURE 58 increases with increasing electron temperature. The APPENDIX shows that the electron impact ionization σv decreases with increasing electron energy above 200 eV. The total beam trapping power decreases with the decreasing cross section and density (see FIGURE 59). In addition, the higher the electron temperature, the greater the electron endloss power (increasing from 10 kW to 70 kW). There is a small decrease in the ion endloss power from 26 kW to 8 kW since the total ion density decreases. The total system energy has also decreased as the electron temperature is increased. Although the power loss through charge exchange with neutral gas decreases from 4.3 kW to 2.4 kW, the fraction of the total system energy lost actually increases. The plasma radius remains relatively constant as the electron temperature increases while the global confinement time increases slightly from 2.2 ms to 2.7 ms. However, $n\tau_p$ decreases as the electron temperature increases. The combination of increased electron endloss and decreasing electron impact ionization as well as an enlarging of the ion loss cone produces a lower density plasma.

The average and peak deuterium density profiles for the various electron temperatures are shown in FIGURES 60-61. The same qualitative behavior of density buildup with fixed electron temperature can be seen. Again the lower density profiles have a correspondingly large neutral density as shown in FIGURE 62. Increasing T_e increases the electron endloss (from 10 kW to 20 kW) with only a slight decrease in the ion endloss (from 2.1 kW to 1.6 kW). Again the beam trapping (FIGURE 63) and beam charge exchange power (from 2.2 kW to $\sim$ 0 kW) is seen to decrease while there is also a small decrease in the power lost from charge exchange with the neutral gas (from 2.9 kW to 2.0 kW).

As for the case of hydrogen, the plasma radius is insensitive to the fixed electron temperature and although there is a slight increase in the global confinement time from 1.7 ms to 2.3 ms there is an overall decrease in $n\tau_p$ with increasing electron temperature. It appears that for buildup in density in the plug, there is no advantage in heating the electrons to energies above 100 eV. The ion energy, being at 10 keV is not affected by these relatively low electron temperatures. In addition, the decrease in the electron impact ionization and increase in both the electron endloss and

enlargement of the ion loss cone boundary tends to inhibit the density buildup.

CONCLUSION

We have first examined the beam divergence and electric field at the emitter surface for a 20 keV hydrogen and a 25 keV deuterium neutral beam source. We have shown that there does not have to be a repositioning of the grid system when 25 keV deuterium is used in a source originally designed for 20 keV hydrogen. However there will be a slight increase in the beam divergence of 20%. We have examined the beam divergence as both the source electron and ion temperatures are varied as well as the electrode positions. We have seen that a higher beam current density results in a smaller beam divergence. For a given set of electrode positions, there is an optimal beam current density. For hydrogen with a current density of .390 A/cm2, the beam rms beam divergence is .0185 radians which increases to .0240 radians when 25 keV deuterium is used. The electric field near the electrodes appear to be low enough so that breakdown or arcing should not occur. In addition, the change in beam divergence with change in species and voltage agrees with the space-charge current limit (see EQUATION 3). From the neutral beam source viewpoint, there is little change in going from 20 keV hydrogen to 25 keV deuterium beams.

We next examined the density buildup of a TARA plug using a 2-D in velocity space, 1-D in real space, time-dependent radial Fokker-Planck code. We observed that with the larger finite Larmor radius of 25 keV deuterons, the plasma is broader but not as dense at the same point in time. We found that the plasma builds up faster when the beam current is increased while an increase in beam energy results in less beam trapping with a resultant decrease in plasma density. A hydrogen plasma can buildup with a higher neutral edge pressure since its density profile is narrower and results in a better screening of neutrals from the center. An edge density at 4 ms in the range of 10^{-6} Torr can be tolerated for a deuterium plasma with 10^{-5} Torr range for a hydrogen plasma. In both cases, a beam displaced 3 cm above the midplane produces a reasonably peaked plasma profile. It appears that heating

the electrons above 100 eV does not improve the density buildup and may actually degrade it due to enhanced electron end losses and enlargement of the ion loss cone.

We can conclude that for TARA more current and lower beam energy results in a higher density, although lower temperature plasma.

LIST OF REFERENCES

[1] Lyman Spitzer Jr., Physics of Fully Ionized Gases, 2nd Edition, (1962), p. 133.

[2] Lyman Spitzer Jr., Physics of Fully Ionized Gases, 2nd Edition, (1962), p. 135.

[3] W. S. Cooper, K. Halboch, S. B. Magyary, Proc. of the Symp. on Ion Sources and Function of Ion Beams, (Berkeley, 1974), LBL 3399 paper II-1.

[4] W. S. Cooper, A. C. Paul, Wolf a Computer Ion Bear Simulation Package (unpublished) August 1976.

[5] A. M. Futch, A Computer Model for the Plasmas Confined by Magnetic Mirror Fields (unpublished).

[6] J. Kesner, B. McVey, R. Post, D. Smith, Construction of TARA Tandem Mirror Facility with an Ion Anchor, (Nov. 1980), (Rev. March 1981).

[7] D. Blackfield and B. Blackwell, 5th Topical Conference on RF Heating, (Madison, 1983).

[8] D. Blackfield and J. Scharer, Nuclear Fusion, (Jan. 1982).

[9] A. A. Mirin, LLL Report UCRL-51615 Rev. 1 (Feb. 1925).

[10] G. D. Kerbel, 5th Topical Conference on RF Heating, (Madison, Feb. 1983).

[11] S. A. Self, Phys. of Fluids 6 (Dec. 1963), p. 1762-1768.

[12] J. Coleman, R. Torti, Private Communication.

[13] J. Conrad, Rev. Sci. Instrum. 51 (4), (Apr. 1980), p. 418-424.

[14] Kesner and Post, Private Communication.

APPENDIX

The buildup code uses the following analytic expression for the charge exchange of atomic hydrogen

$$\sigma_{cx} = \frac{0.6937\times10^{-14}\left[1 - 0.155\ \log_{10}(E/p)^{2}\right]}{1 + 0.1112\times10^{-14}\ (E/p)^{3.3}} \qquad \text{(A-1)}$$

where E is the ion energy in eV and P is the ratio of the hydrogen species' mass to the proton mass.

FIGURE A-1 shows the charge exchange cross section for ion energies from 1 keV to 50 keV for both hydrogen (solid curve) and deuterium (dashed curve).

The ion impact ionization cross section is given by

$$\sigma_i = z^2\ 10^{-\left[0.8712[\log_{10}(E/p)]^2 - 8.156\ \log_{10}(E/p) + 34.833\right]} \qquad \text{(A-2)}$$

where $E \leq 150$ keV. FIGURE A-2 shows the cross section for both hydrogen (solid) and deuterium (dahsed).

The total trapping cross section plotted in FIGURE A-3 for hydrogen and deuterium is comprised of charge exchange and ion and electron impact ionizations. From FIGURE A-3 we see that for hydrogen energies below 30 keV, the trapping σv is higher. On comparing the trapping of 20 keV hydrogen beams with 25 keV deuterium beams, we first notice that trapping σv for 20 keV hydrogen and 25 keV deuterium are nearly equal. However, the trapping σv for the half and third energy beams components are higher for hydrogen. For the same initial target density, one would expect a higher density buildup using a 20 keV hydrogen beam.

FIGURE A-4 shows that the charge exchange σv for hydrogen is higher at the lower energies compared with deuterium. However, charge exchange merely

replaces a plasma ion with a beam ion, the total ion density remaining constant. FIGURE A-5 explains the difference in trapping behavior between hydrogen and deuterium. For all three components of the 20 keV hydrogen beam the ion impact ionization σv is larger. The increase in ion impact ionization produces the higher density in hydrogen.

Finally we can partially explain the behavior buildup with the assumed electron temperature by examining the electron impact ionization σv. The electrons are assumed to be Maxwellian with a velocity much greater than the ion velocity. Consequently, the ion can be assumed to be at rest so there is no ion mass dependence in the electron impact ionization cross section. The σv is therefore a function only of the electron energy and is given by

$$\langle \sigma v \rangle_e = A[1 - e^{-0.00074E^2}] + BE - CE^2 \qquad \text{(A-3)}$$

where $A = 2.9297 \times 10^{-8}$; $B = 0.246862 \times 10^{-10}$; $C = 5 \times 10^{-14}$ for $E \leq 450$ eV

$$\langle \sigma v \rangle_e = \frac{A}{E^{1/2}} [\ln E + B] \qquad \text{(A-4)}$$

where $A = 1.62 \times 10^{-7}$ and $B = 2.0618$ for $E > 450$ eV.

For E = 100 eV, the electron impact ionization $\langle \sigma v \rangle = 3.2 \times 10^{-8}$ cm³/s for all ion energies between 1 and 50 keV. This σv is comparable to that of the ion impact ionization σv. Since charge exchange does not change the plasma density and ion impact ionization is not a function of the electron temperature raising T_e decreases the electron impact ionization hence decreasing the beam trapping. In addition, since the electron impact ionization is not a function of ion mass, the increase in density with hydrogen can be partially explained by the higher ion impact ionization cross section at lower energies.

TABLE 1

FORMULA	UNITS	H	D	D
Mass	M_{proton}	1	2	2
Energy	keV	20	25	20
$f_{ci} \propto m^{-1/2}$	MHz	6	3	3
$V_{thi} \propto (Em)^{1/2}$	cm/sec	1.95×10^{8}	1.56×10^{8}	1.39×10^{8}
$\rho_i \propto (E/m)^{1/2}$	cm	3.62	5.73	5.13
$V_A \propto m^{-1/2}$	cm/sec	6.16×10^{8}	4.3×10^{8}	4.3×10^{8}
$C_s \propto (T_e/m)^{1/2}$	cm/sec	2.4×10^{7}	1.7×10^{7}	1.7×10^{7}
$f_{pi} \propto m^{-1/2}$	MHz	296	210	210
$\tau_{90^o} \propto m^{1/2} T^{3/2}$	sec	1	2	1.4
$\tau_s \propto \frac{T^{3/2}}{m^{1/2}}$	sec	.52	1.0	.73
$\tau_{eq} \propto m^2 T^{3/2}$	sec	.95	2.7	1.9
σ_{cx}(See Appendix)	cm^2	6.6×10^{-16}	8.9×10^{-16}	9.84×10^{-16}
σ^i_{ion}(See Appendix)	cm^2	1.4×10^{-16}	9.1×10^{-16}	7.1×10^{-17}
$\langle\sigma v\rangle_{cx}$(See Appendix)	cm^3/sec	1.28×10^{-7}	1.39×10^{-7}	1.36×10^{-7}
$\langle\sigma v\rangle^i_{ion}$(See Appendix)	cm^3/sec	2.63×10^{-8}	1.4×10^{-8}	9.84×10^{-9}
$\langle\sigma v\rangle^e_{ion}$(See Appendix)	cm^3/sec	3.4×10^{-8}	3.4×10^{-8}	3.4×10^{-8}
space charge $J \propto \frac{V^{3/2}}{m^{1/2}}$	ratio to 20 keV H	1	.988	.707
Neutral Beam RMS divergence	radians	.0236	.0277	----

TABLE 2

25 keV Deuterium Neutral Beam Base Case

Mesh points in x-direction	65
Mesh points in y-direction	15
Width of grid	.381 cm
Length of grid	.98 cm
Extractor grid voltage	25 keV
Acel grid voltage	-2 keV
Decel grid voltage	0 keV
Distance from extractor to acel	.64 cm
Distance from acel to decel	.21 cm
Desired electric field at emitter surface	300 V/cm
Position of beam divergence measurement	.9712 cm
Number of beams	15
Number of beamlets per beam	5
Initial ion v_x	(-.361, -.139, 0., .139, .361) × 3.9×10^6 cm/sec
Initial ion v_y	(1.0) × 3.9×10^6 cm/sec
Plasma T_e	15 eV
RMS beam divergence	.0277 radians
Current density	.390 A/cm^2

TABLE 3

Buildup Base Cases

	H	D
Bfield (Gauss)	4000	4000
Mirror ratio	2.5	2.5
Initial plasma radius	14.5 cm	14.5 cm
Plug length	26 cm	26 cm
Radial mesh points	30	30
Ion velocity mesh points	40	40
Electron velocity mesh points	101	101
Initial anbipolar potential (eV)	300	300
E_e (keV)	.150	.150
E_i (keV)	10	10
mass (m/m_H)	1	2
Beam injection energies (keV)	20;10;6.7	25;12.5;8.3
Beam current density ($\times 1.372\times10^{18} cm^{-2} sec^{-1}$)	1:2/3:1	1:2/3:1
Total "effective" current (Amps)	100	100
Total "effective" power (MW)	1.25	1.56
Initial $n_e(0)$ (cm^{-3})	1.8×10^{12}	1.4×10^{12}
Initial n_e (cm^{-3})	6.0×10^{11}	4.4×10^{11}

TABLE 3 -- CONT'D

	At t=4ms	
	H	D
$n_e(0)$ (cm^{-3})	2.1×10^{13}	6.3×10^{12}
n_e (cm^{-3})	5.7×10^{12}	2.2×10^{12}
τ_p (ms)	2.2	1.7
R_p (cm)	14.0	14.7
P_{trap} (kW)	143	32
P^{cx}_{beam} (kW)	13	2
P^{cx}_{gas} (kW)	4.8	3
$P^{i}_{endloss}$ (kW)	23.5	2
$P^{e}_{endloss}$ (kW)	9	7
$n_{neutral}$ (0) (cm^{-3})	2.5×10^{6}	1×10^{8}
36	.0277	---

ACKNOWLEDGEMENTS

I have received a great amount of assistance from several people in the course of producing this work. Dr. Conrad at Wisconsin introduced me to the Wolf code and helped with the initial neutral beam source design while Carol Tull at the MFECC assisted in converting the code to run on the CRAY. Drs. Coleman and Torti at MIT, scientists in the TARA neutral beam group provided much guidance throughout the WOLF study. Dr. Futch at LLNL gave me the buildup code and was always helpful in answering my questions. I often consulted with Dr. Kesner, TARA theory leader at MIT and compared my results with those obtained by Dr. Horne at Wisconsin. I would also like to acknowledge the support of Dr. Post, the leader of the TARA project who suggested that I undertake this study. Finally this report would not have been possible without the help provided by Beth, Elaine and Dorothea who typed this paper and put up with my constant revisions (the curse of word processing).

LIST OF FIGURES

Fig. 14 Initial ion energy profiles for hydrogen and deuterium.

Fig. 15 Time evolution of both the ion density and energy profiles for the base hydrogen case (20 keV hydrogen beams).

Fig. 16 Time evolution of both the ion density and energy profiles for the base deuterium case (25 keV deuterium beams).

Fig. 17 Time evolution of the Franck-Condon neutral profiles for both base cases.

Figures 18-60 are at t = 4 ms with the ratio of full to half to third energy components being 1:2/3:1.

Fig. 18 Hydrogen ion density profiles for various neutral beam positions.

Fig. 19 Hydrogen ion energy profiles for various neutral beam positions.

Fig. 20 Hydrogen Franck-Condon neutral profiles for various neutral beam positions.

Fig. 21 Average electron density versus beam positioning for 20 keV hydrogen beams.

Fig. 22 Total trapping power for 20 keV hydrogen beams (1.25 MW, 100A) for various beam positions. For d = 10.5 cm, beam is close to plasma edge.

Fig. 23 Charge exchange with cold neutral gas power loss for 20 keV hydrogen beams (1.25 MW, 100A) for various beam positions.

Fig. 24 Average electron density versus beam positioning for 25 keV deuterium beams.

Fig. 25 Deuterium ion density profiles for various neutral beam positions.

Fig. 26 Deuterium ion energy profiles for various neutral beam positions.

Fig. 27 Deuterium Franck-Condon neutral profiles for various neutral beam positions.

Fig. 28 Power loss through charge exchange with cold neutral gas for various deuterium neutral beam positions.

Fig. 29 Total trapping power for 25 keV deuterium beams (1.56 MW, 100 A) for various beam positions.

Fig. 30 Hydrogen ion density profiles for various neutral beam currents (50 A, 75 A, 100 A, 125 A and 150 A).

Fig. 31 Average electron density for various 20 keV hydrogen beam currents.

Fig. 32 Total beam trapping power for various 20 keV hydrogen beam currents (0.62 MW, 0.94 MW, 1.25 MW, 1.56 MW and 1.87 MW).

Fig. 33 Franck-Condon hydrogen neutral profiles for various 20 keV hydrogen beam currents.

Fig. 34 Power lost through charge exchange with cold gas for various 20 keV hydrogen beam currents.

Fig. 35 Global hydrogen ion particle confinement time for various 20 keV hydrogen beam currents.

Fig. 36 Deuterium ion density profiles for various neutral beam currents (50 A, 75 A, 100 A, 125 A and 150 A).

Fig. 37 Average electron density for various 25 keV deuterium beam currents.

Fig. 38 Franck-Condon deuterium neutral profiles for various 25 keV deuterium beam currents.

Fig. 39 Power lost through charge exchange with cold gas for various 25 keV deuterium beam currents.

Fig. 40 Total beam trapping power for various 25 keV deuterium beam currents (0.78 MW, 1.17 MW, 1.56 MW, 1.95 MW and 2.34 MW).

Fig. 41 Hydrogen ion density profiles for 100 A hydrogen neutral beam with various energies (15 keV, 20 keV, 25 keV and 30 keV).

Fig. 42 Average hydrogen ion density for various neutral beam energies.

Fig. 43 Hydrogen ion energy profiels for 100 A hydrogen neutral beam with various energies.

Fig. 44 Hydrogen Franck-Condon neutral profiles for 100 A hydrogen neutral beam with various energies.

Fig. 45 Deuterium ion density profiles for 100 A deuterium neutral beam with various energies (15 keV, 20 keV, 25 keV and 30 keV).

Fig. 46 Average deuterium ion density for various neutral beam energies.

Fig. 47 Deuterium ion energy profiles for 100 A deuterium neutral beam with various energies.

Fig. 48 Deuterium Franck-Condon neutral profiles for 100 A deuterium neutral beam with various energies.

Fig. 49 Total beam trapping power for 100 A deuterium neutral beams with various energies (1.00 MW, 1.32 MW, 1.56 MW and 2.00 MW).

Fig. 50 Hydrogen ion density profile for 100 A, 20 keV hydrogen neutral beam with various edge pressures from 3.0×10^{-10} Torr to 6.0×10^{-8}.

Fig. 51 Hydrogen Franck-Condon neutral profile for 100 A, 20 keV hydrogen neutral beam with various edge pressures.

Fig. 52 Hydrogen ion energy profile for 100 A, 20 keV hydrogen neutral beam with various edge pressures.

Fig. 53 Deuterium ion density profile for 100 A, 25 keV deuterium neutral beeam with various edge pressures from 1.0×10^{-10} Torr to 6.0×10^{-8}.

Fig. 54 Average electron density for 100 A, 25 keV deuterium neutral beam with various edge pressures.

Fig. 55 Deuterium Franck-Condon neutral profile for 100 A, 20 keV deuterium neutral beam with various edge pressures.

Fig. 56 Hydrogen ion density profile for 100 A, 20 keV hydrogen beam with the electron energy fixed at 100 eV, 200 eV, 500 eV, 750 kV and 1000 eV.

Fig. 57 Average electron density for 100 A, 20 keV hydrogen beam with the electron energy fixed at 100 eV, 200 eV, 500 eV, 750 eV and 1000 eV.

Fig. 58 Hydrogen Franck-Condon neutral profiles for 100 A, 20 keV hydrogen beam with the electron energy fixed at 100 eV, 200 eV, 500 eV, 750 eV and 1000 eV.

Fig. 59 Total beam trapping power for 100 A, 20 keV hydrogen beam with the electron energy fixed at 100 eV, 200 eV, 750 eV and 1000 eV.

Fig. 60 Deuterium ion density profile for 100 A, 25 keV deuterium beam with the electron energy fixed at 100 eV, 200 eV, 500 eV, 750 eV, 1000 eV.

Fig. 61 Average electron density for 100 A, 25 keV deuterium beam with the electron energy fixed at 100 eV, 200 eV, 500 eV, 750 eV and 1000 eV.

Fig. 62 Deuterium Franck-Condon neutral profiles for 100 A, 25 keV deuterium beam with the electron energy fixed at 100 eV, 200 eV, 500 ev, 750 eV and 1000 eV.

Fig. 63 Total beam trapping power for 100 A, 25 keV deuterium beam with the electron energy fixed at 100 eV, 200 eV, 500 eV, 750 eV and 1000 eV.

Figures for Appendix with hydrogen (solid) and deuterium (dotted) curves.

Fig. A-1 Charge exchange cross section.

Fig. A-2 Ion impact ionization cross section.

Fig. A-3 Total beam trapping σv (sum of charge exchange and ion and electron impact ionization σv).

Fig. A-4 Charge exchange σv.

Fig. A-5 Ion impact ionization σv.

Fig. A-6 Electron impact ionization σv versus electron energy.

HYDROGEN

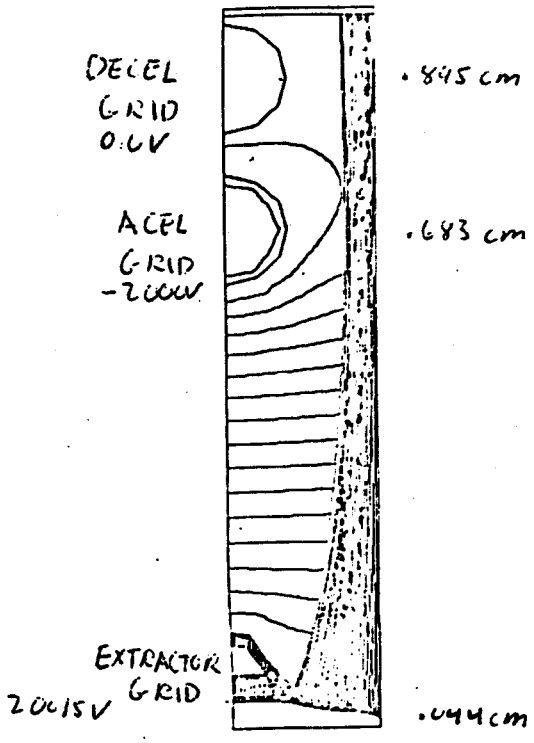

FIG. 1

DEUTERIUM

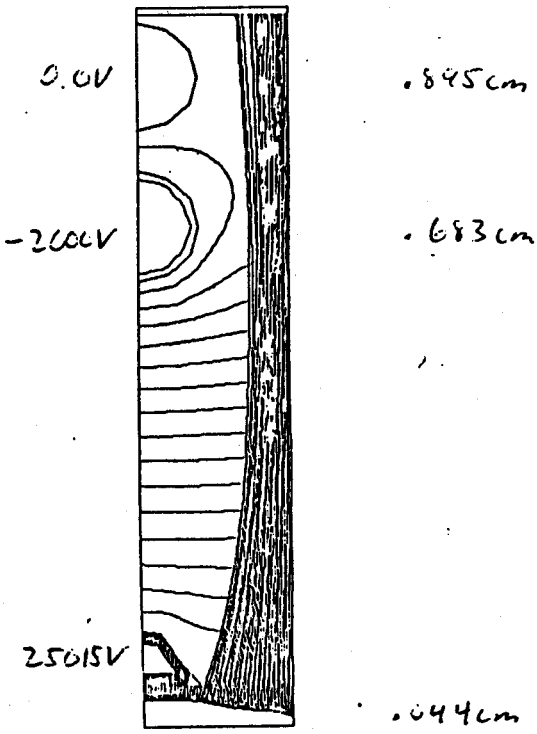

FIG 3

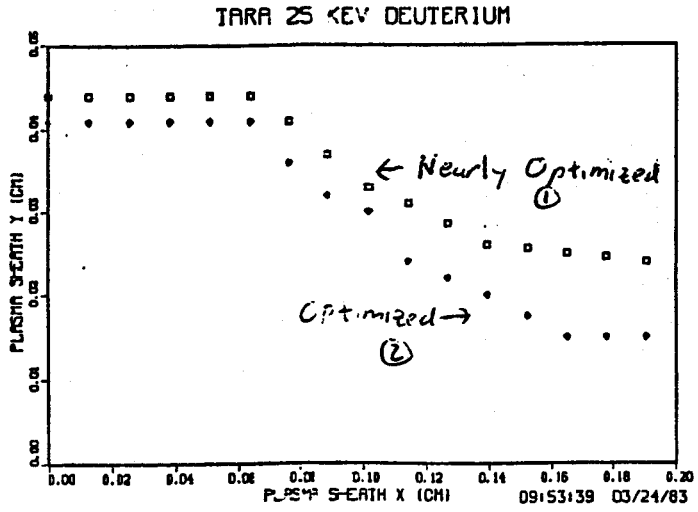

FIG. 2

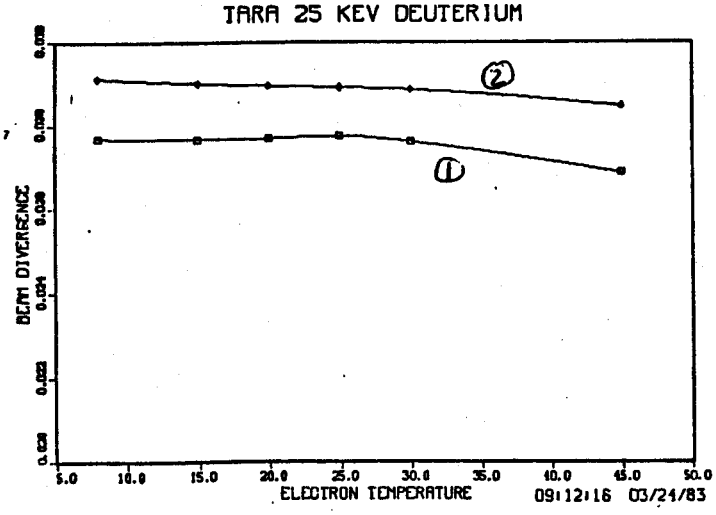

FIG. 4

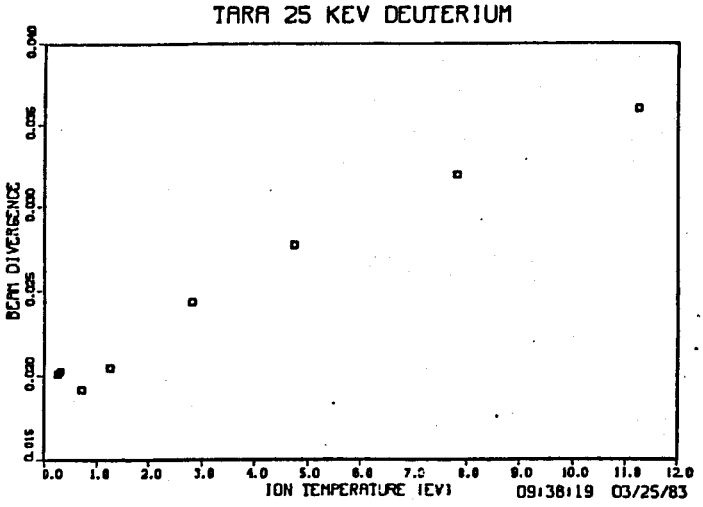

FIG 5

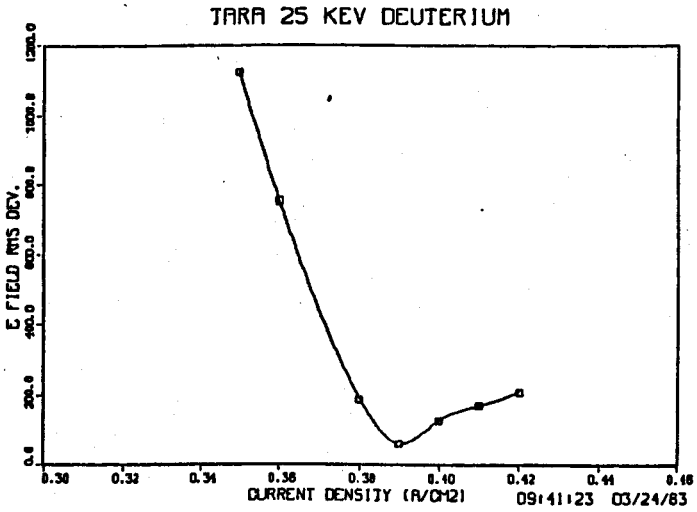

FIG 7

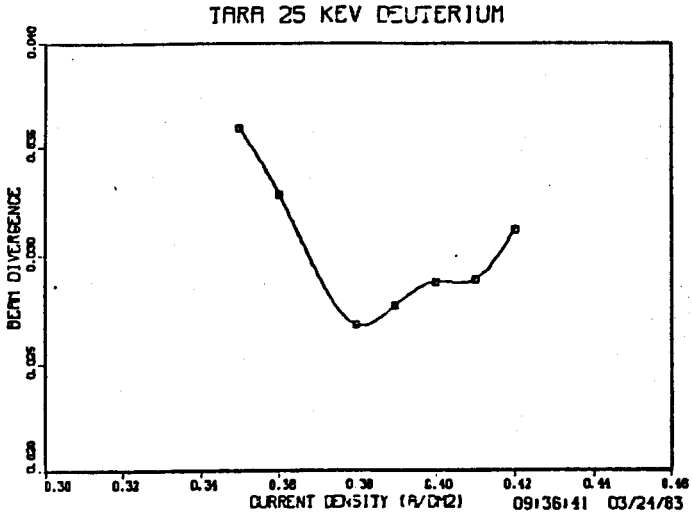

FIG 6

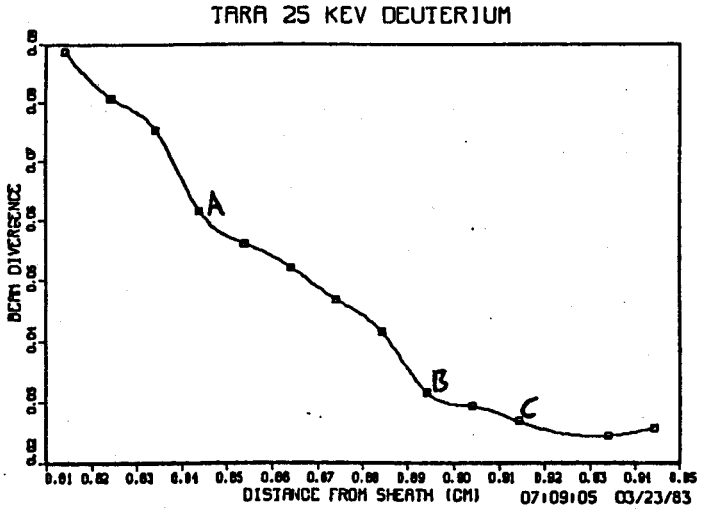

FIG 8

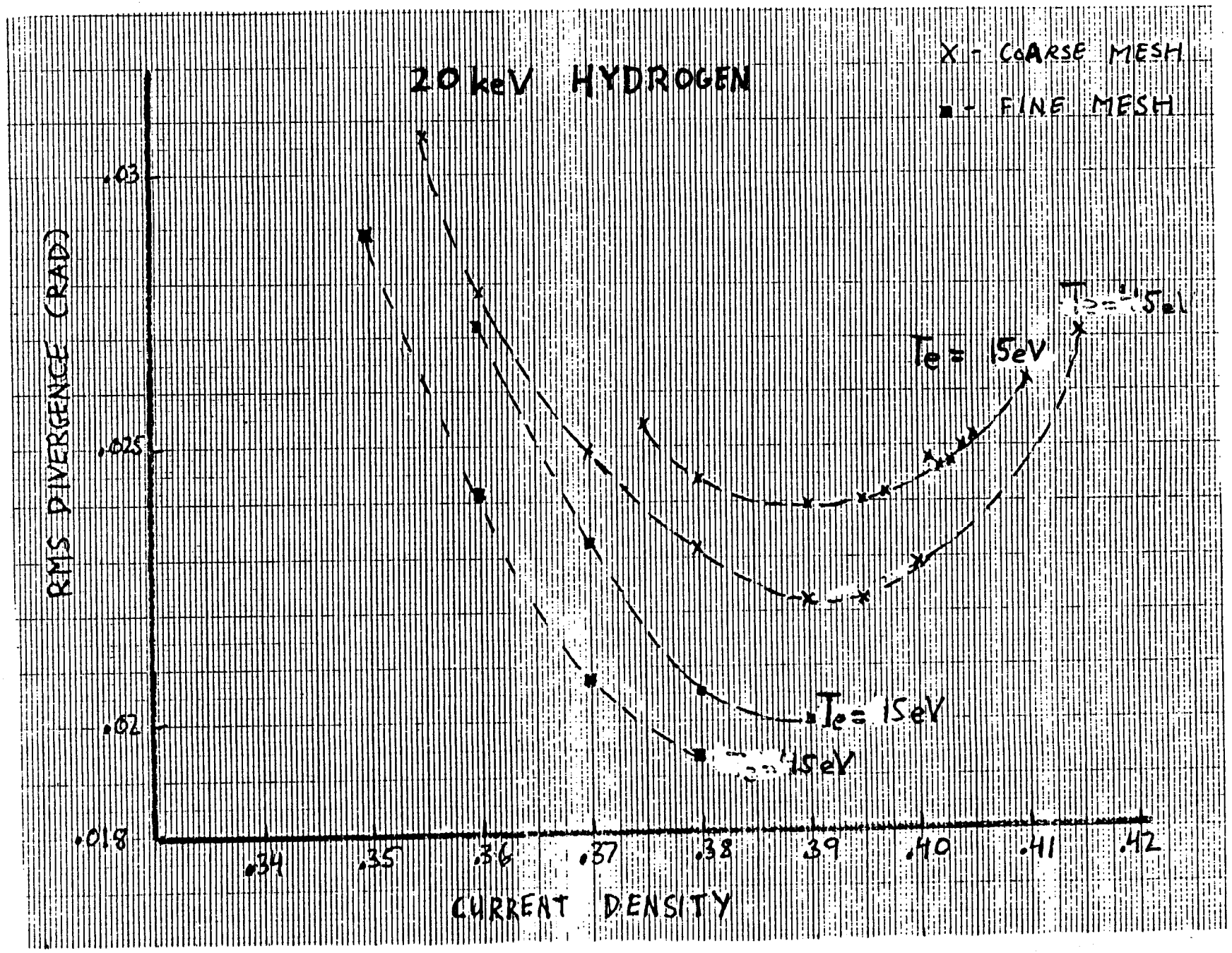
20 keV HYDROGEN
X - COARSE MESH
■ - FINE MESH
RMS DIVERGENCE (RAD)
.03
.025
.02
.018
.34
.35
.36
.37
.38
.39
.40
.41
.42
CURRENT DENSITY
Te = 15eV
Te = 15eV
Te = 15eV

FIG. 11

EDGE NEUTRAL PRESSURE

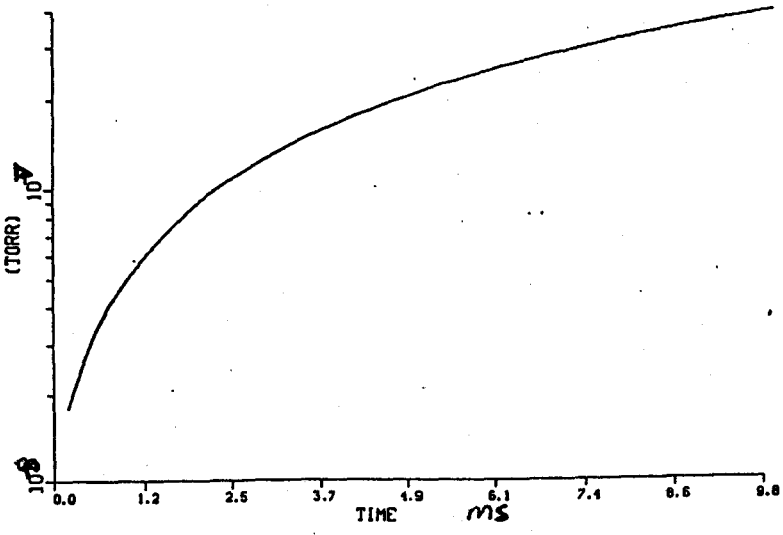

FIG. 12

INITIAL ION DENSITIES

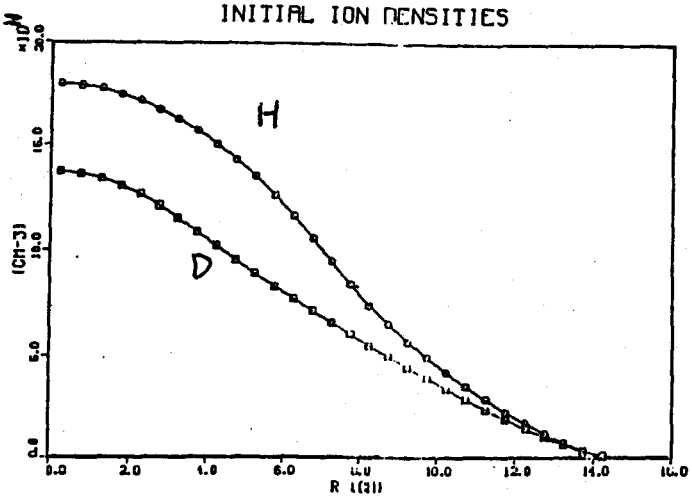

FIG 13

INITIAL ION ENERGIES

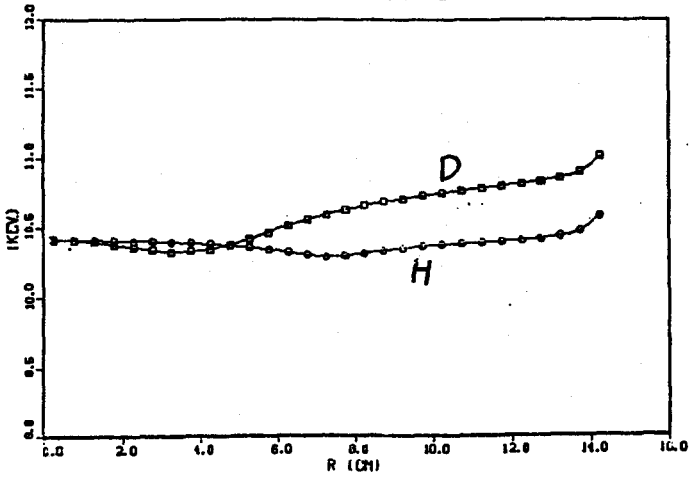

FIG 14

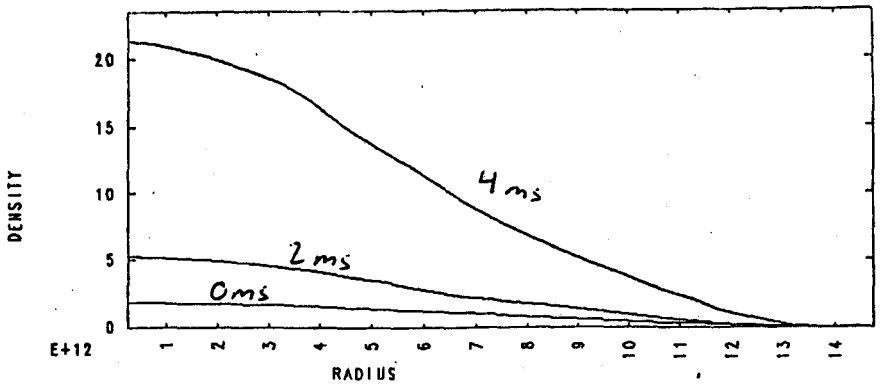

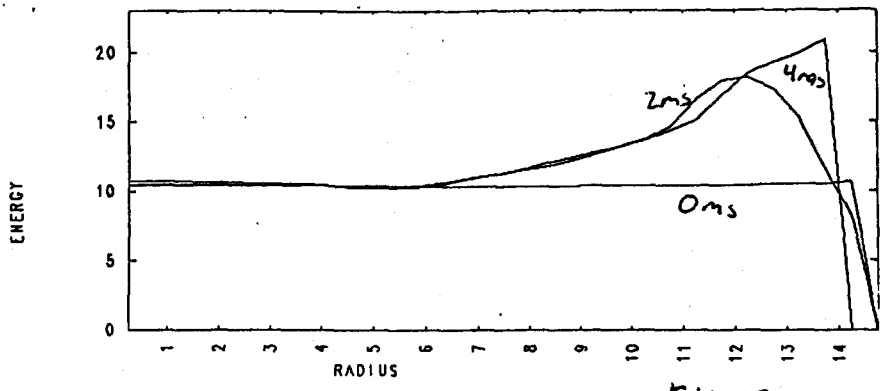

K= 2 HYDROGEN

FIG 15

N= 200 TIME= 4.048000E-03 SEC

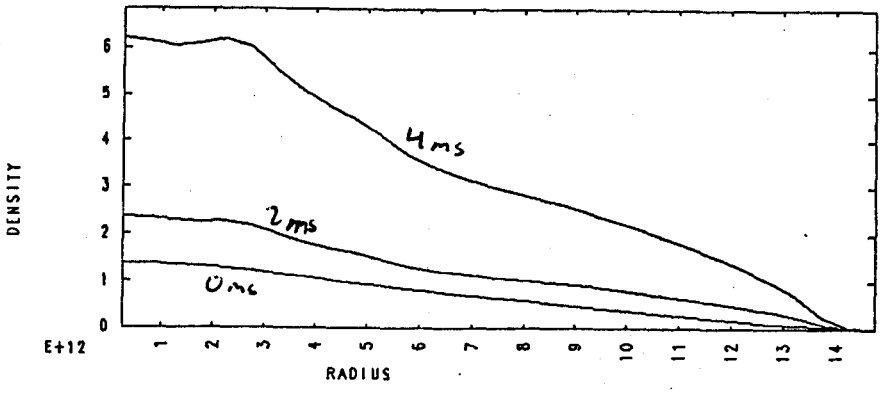

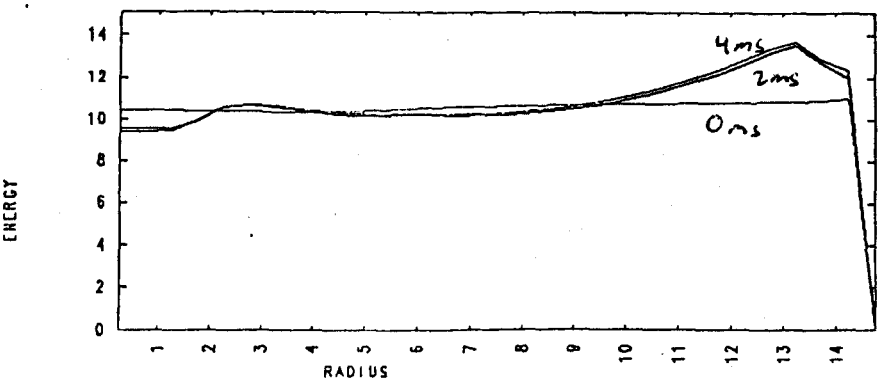

K= 2 DEUTERIUM

N= 200 TIME= 4.048000E-03 SEC

FIG 16

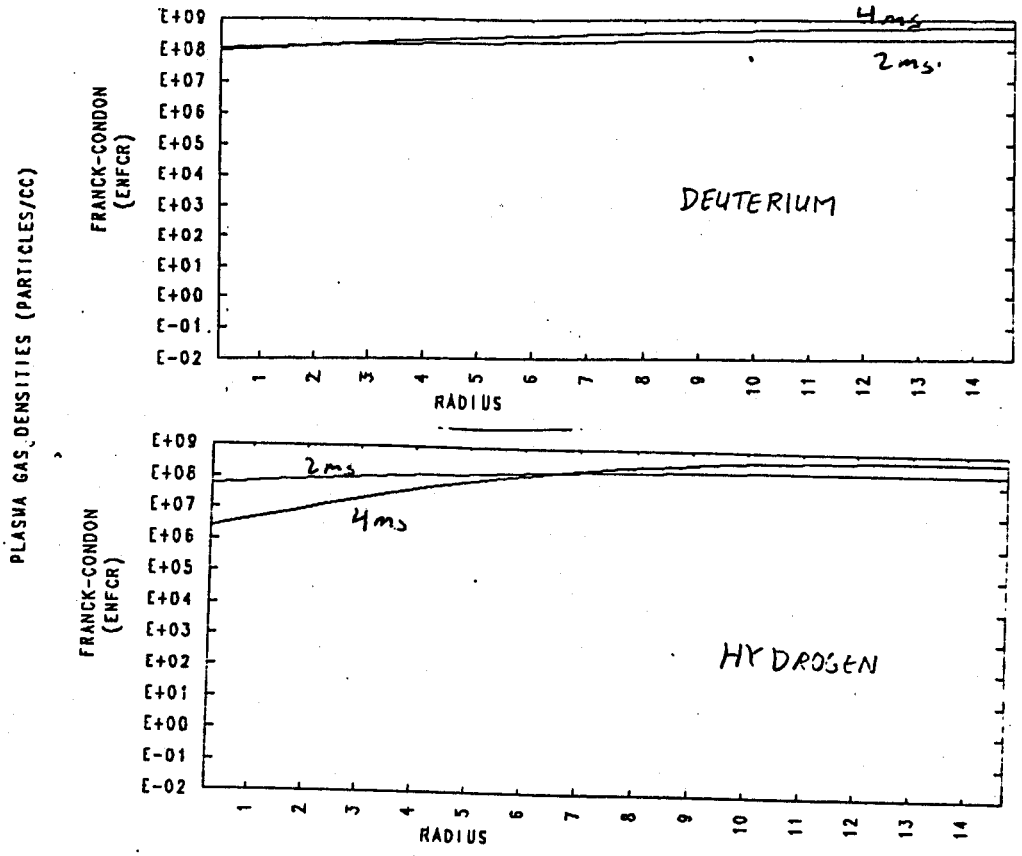
PLASMA GAS DENSITIES (PARTICLES/CC)
FRANCK-CONDON (ENFCR)
E+09
E+08
E+07
E+06
E+05
E+04
E+03
E+02
E+01
E+00
E-01
E-02
4ms
2ms
DEUTERIUM
1 2 3 4 5 6 7 8 9 10 11 12 13 14
RADIUS
FRANCK-CONDON (ENFCR)
2ms
4ms
HYDROGEN
RADIUS
N= 200
TIME= 4.048000E-03 SEC

FIG. 17

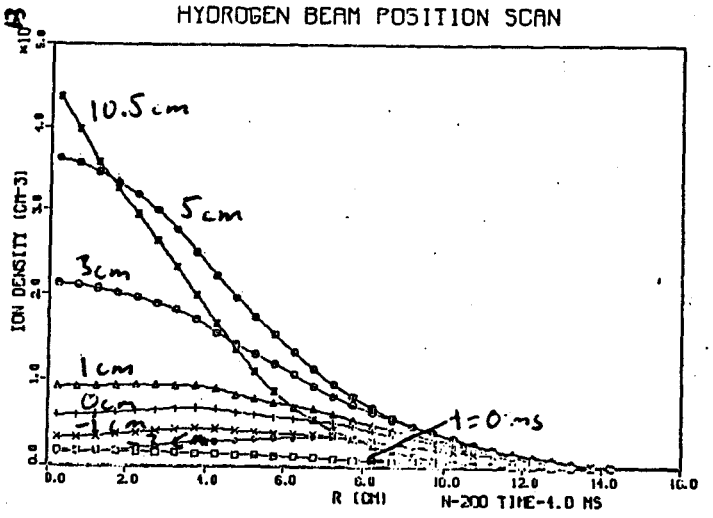

FIG. 18

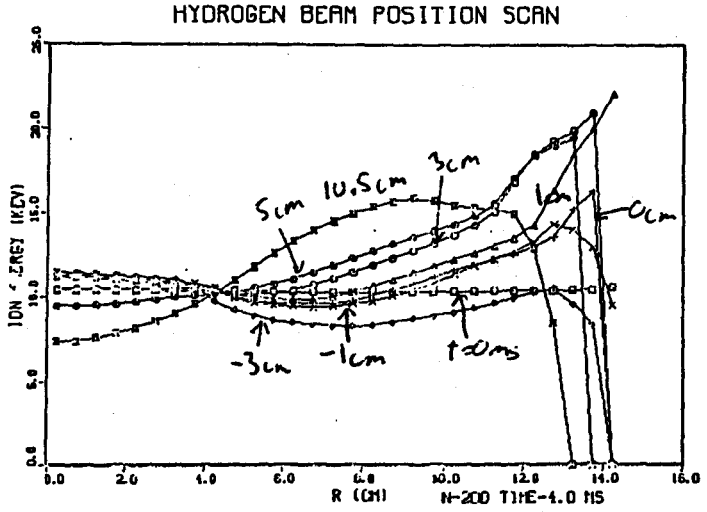

FIG. 19

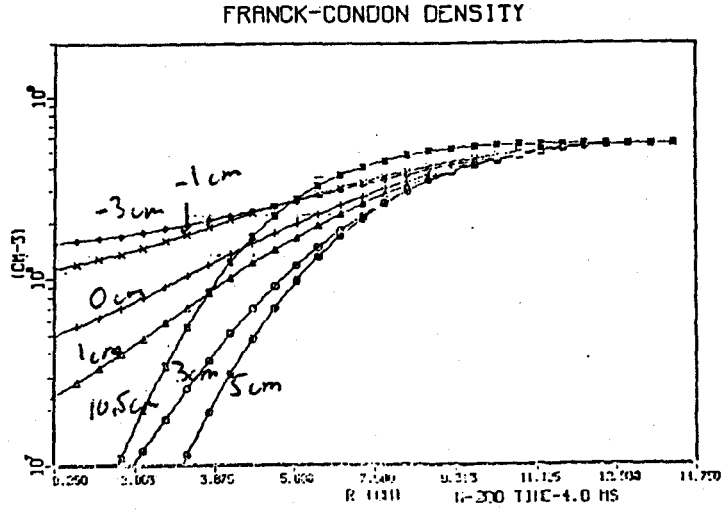

FIG 20

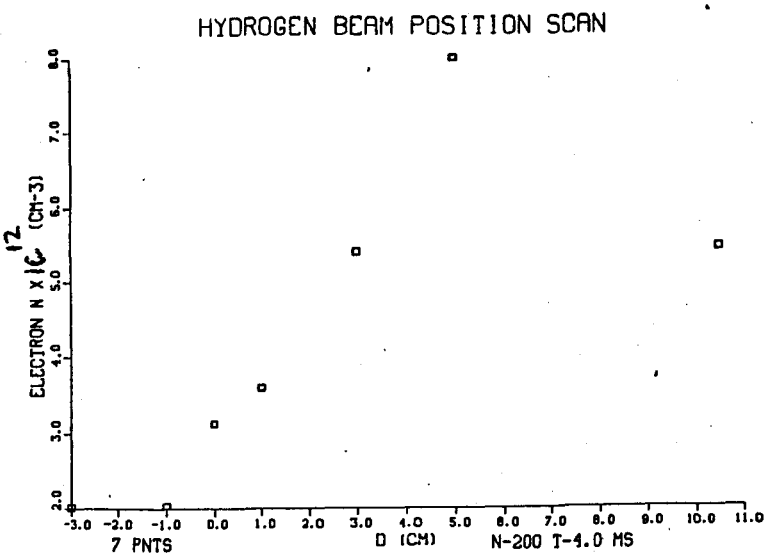

FIG. 21

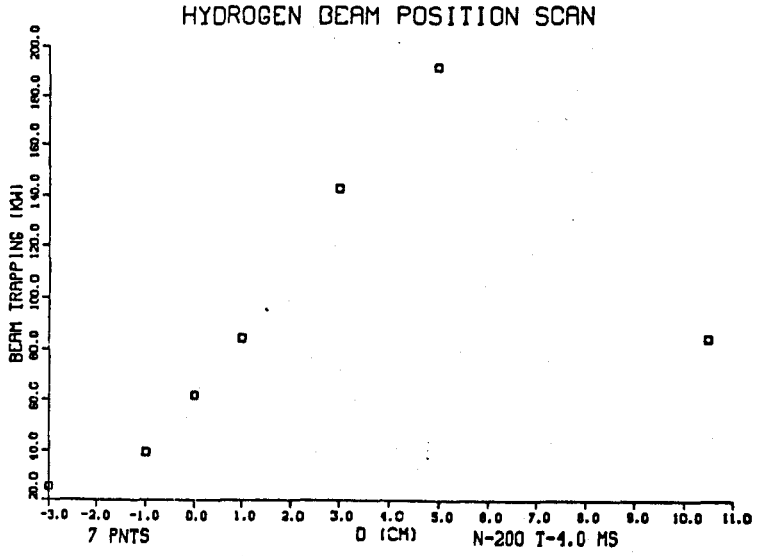

FIG. 22

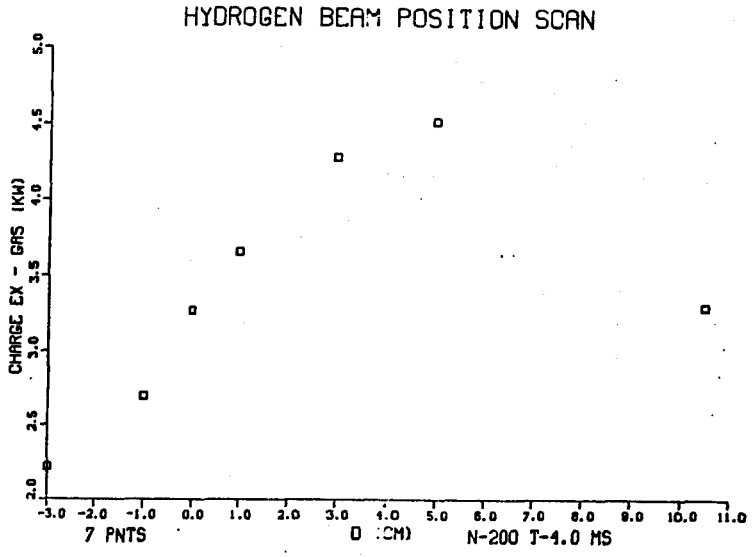

FIG. 23

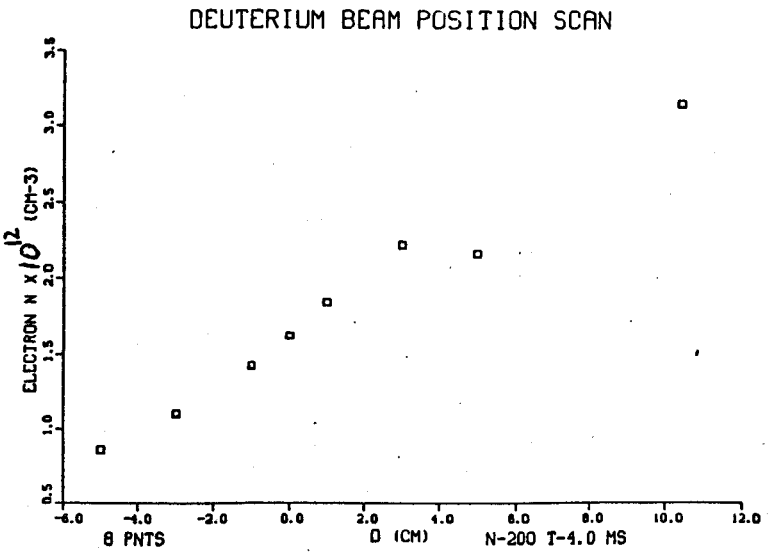

FIG 24

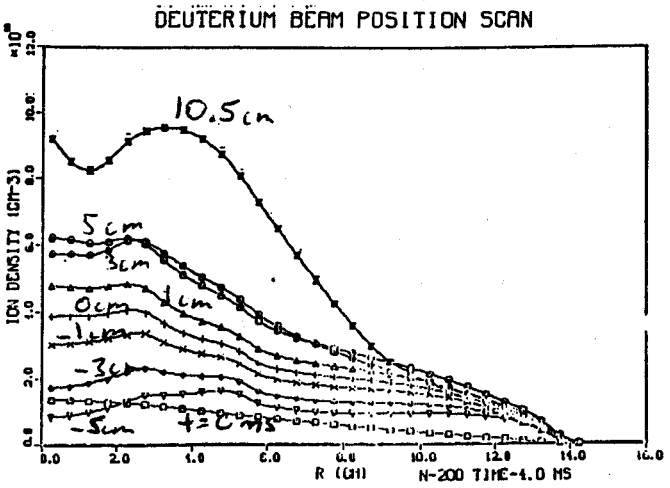

FIG 25

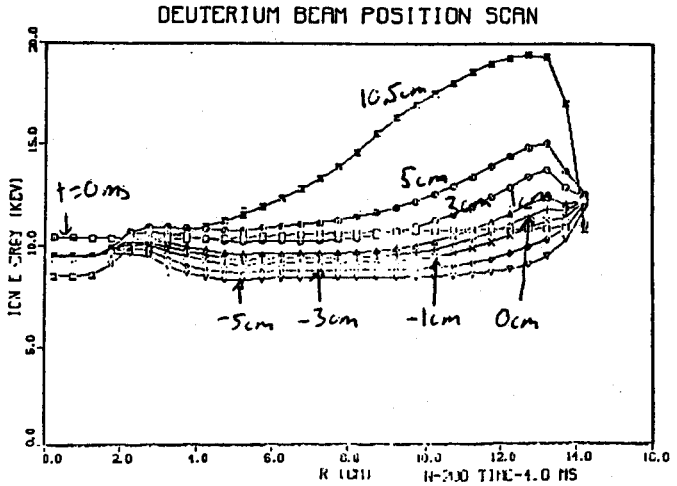

FIG. 26

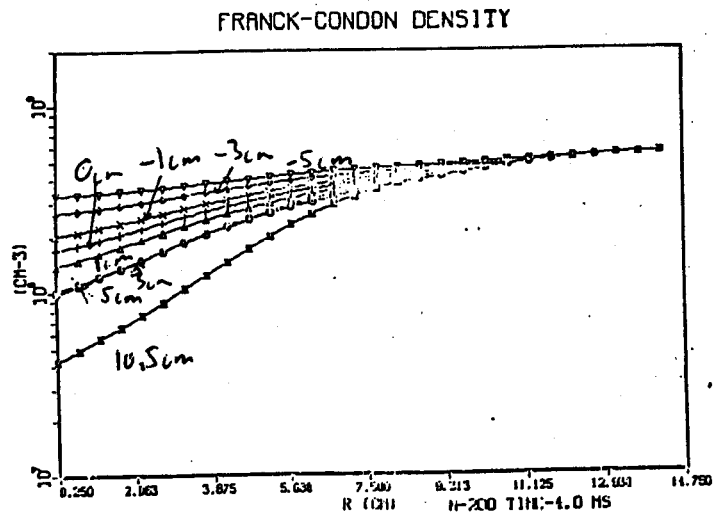

FIG. 27

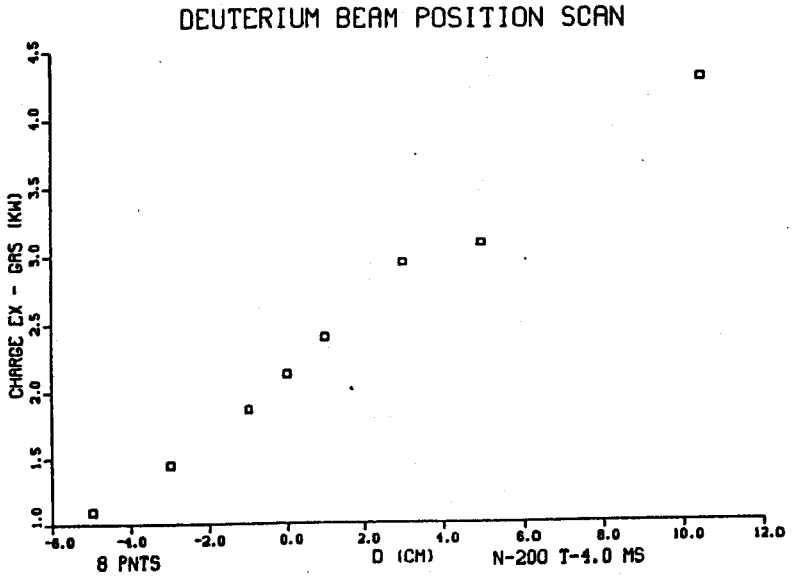

FIG. 28

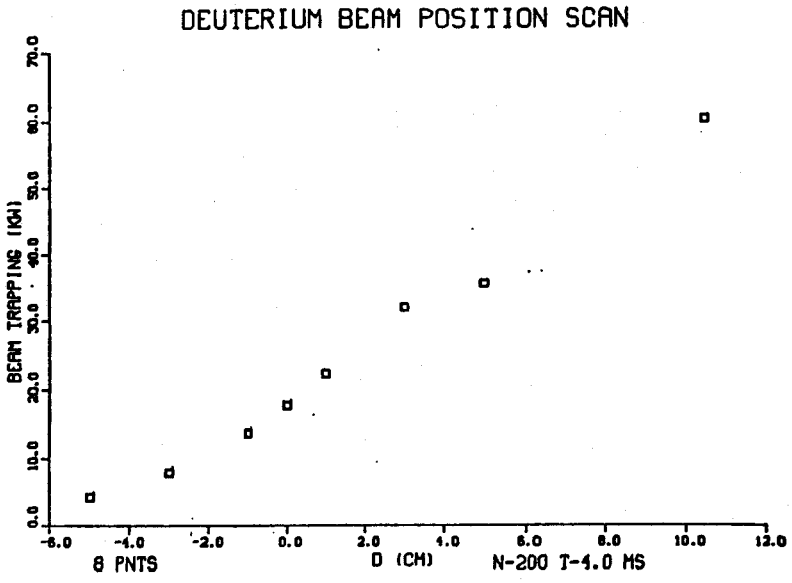

FIG. 29

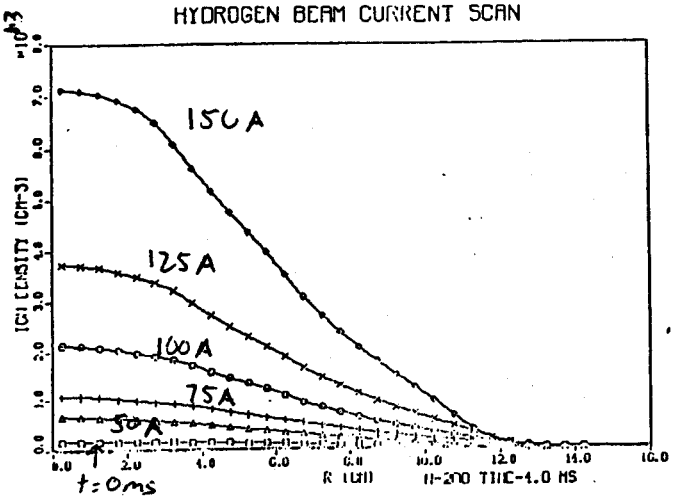

FIG 30

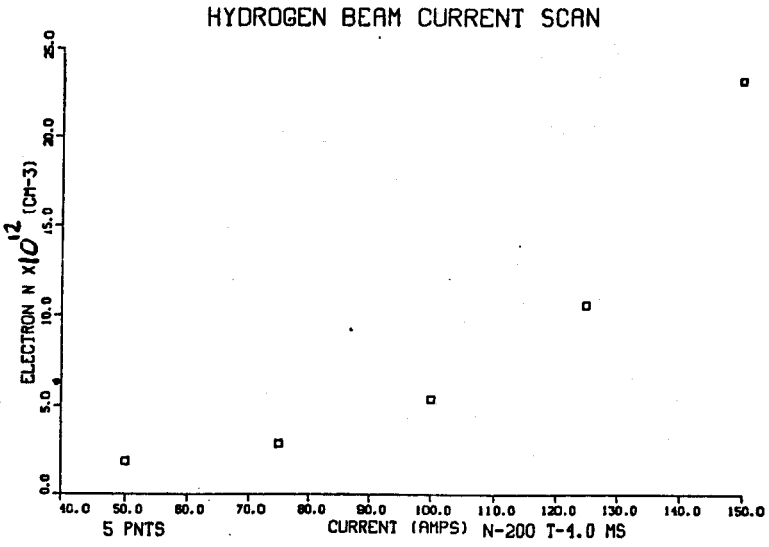

FIG 31

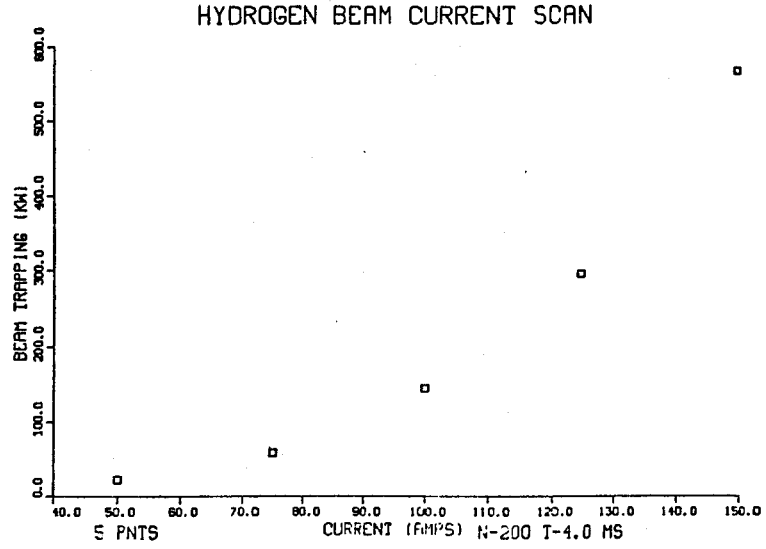

FIG 32

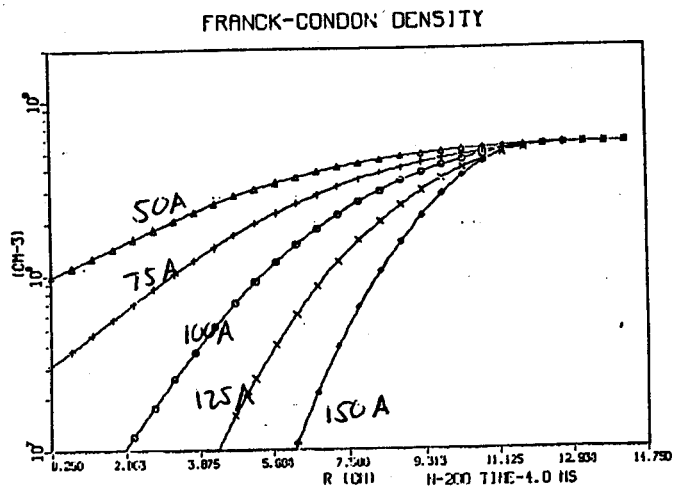

FIG 33

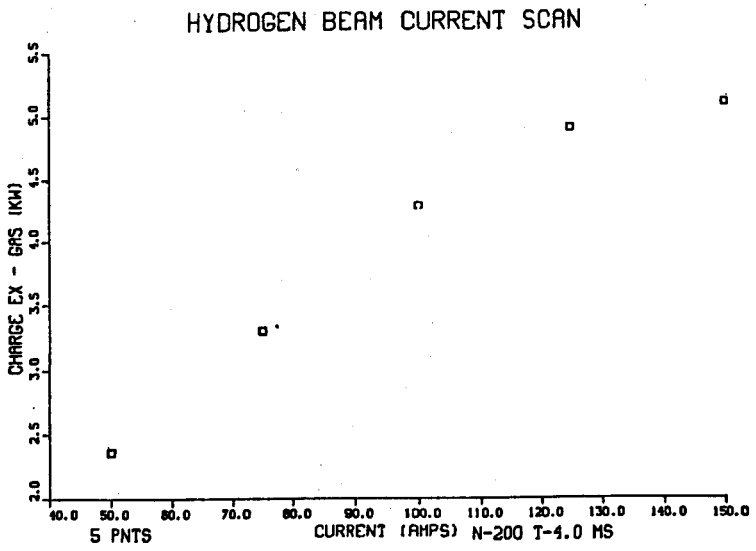

FIG. 34

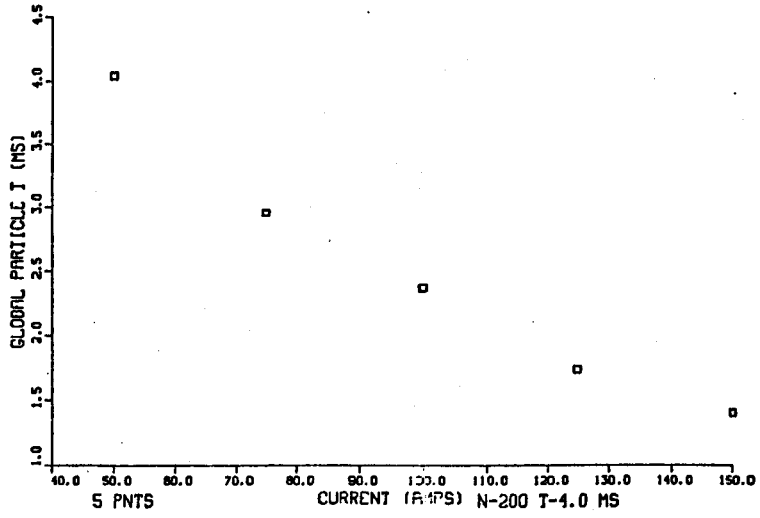

FIG 35

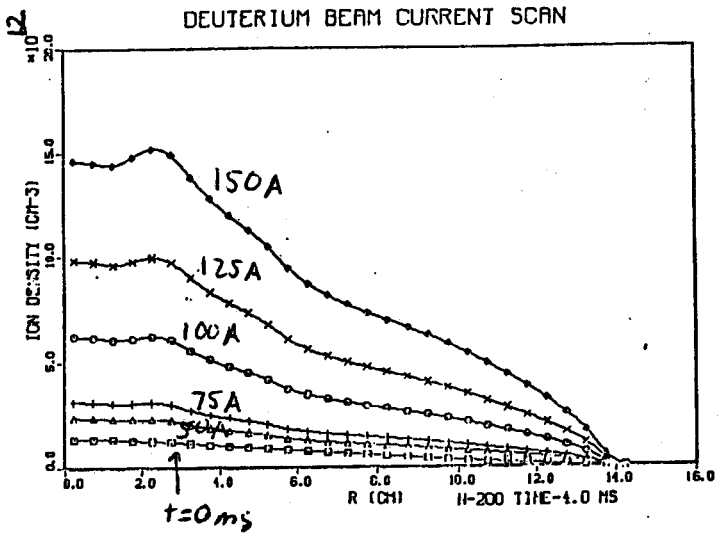

FIG 36

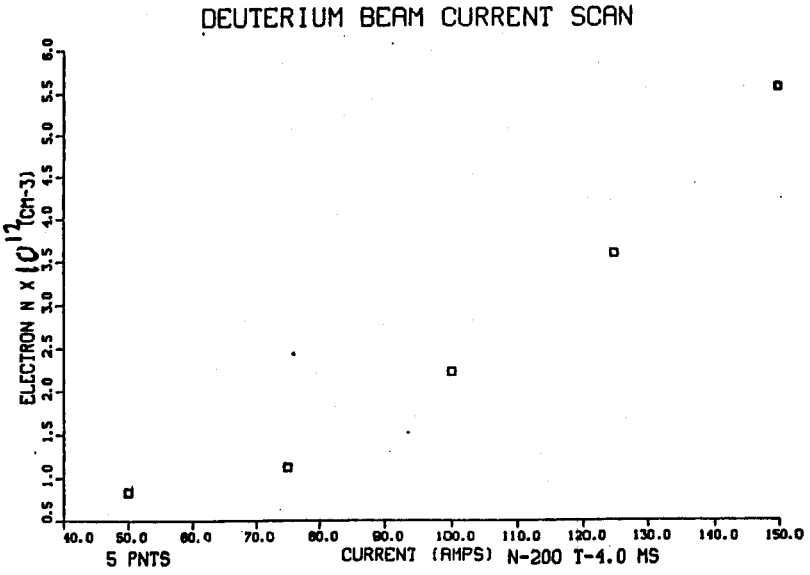

FIG 37

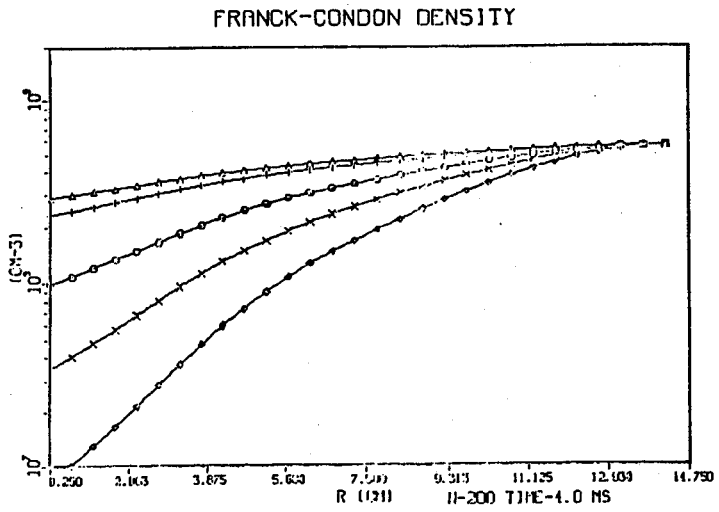

FIG 38

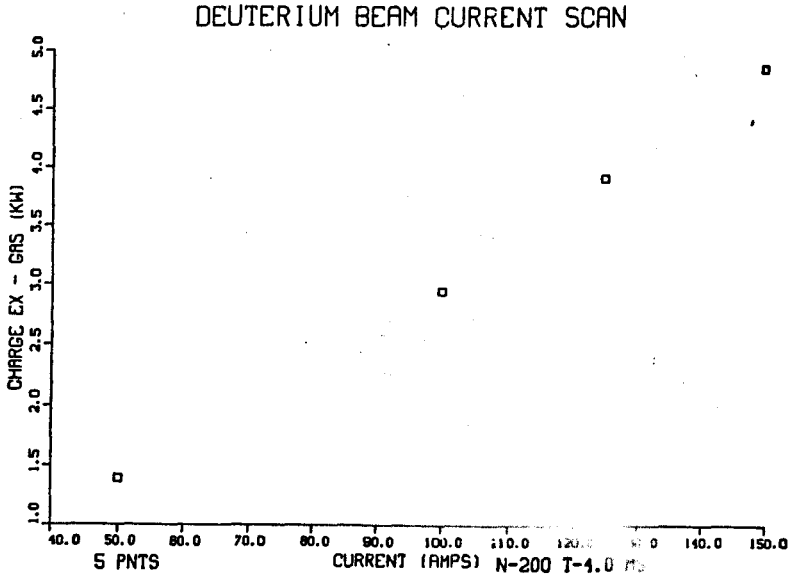
DEUTERIUM BEAM CURRENT SCAN
CHARGE EX - GAS (KW)
1.0
1.5
2.0
2.5
3.0
3.5
4.0
4.5
5.0
40.0
50.0
60.0
70.0
80.0
90.0
100.0
140.0
150.0
5 PNTS
CURRENT (AMPS) N-200 T-4.0

FIG 39

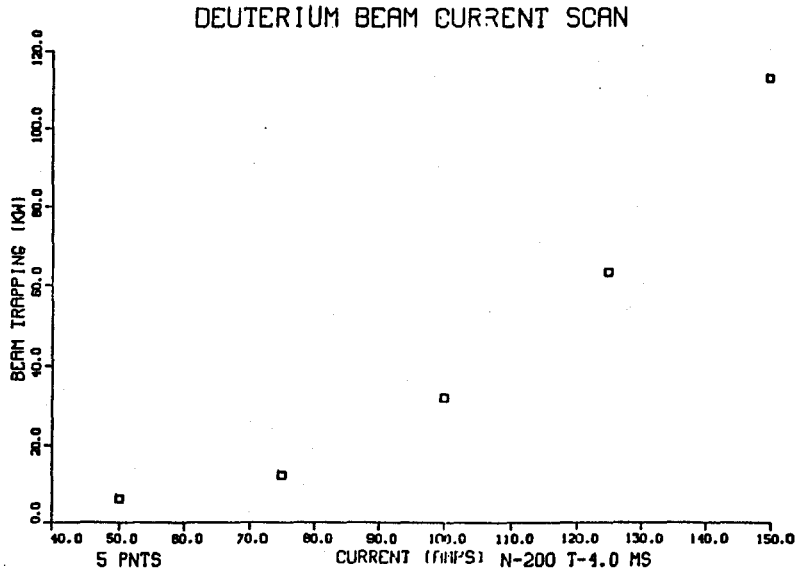
DEUTERIUM BEAM CURRENT SCAN
BEAM TRAPPING (KW)
0.0
20.0
40.0
60.0
80.0
100.0
120.0
40.0
50.0
60.0
70.0
80.0
90.0
100.0
110.0
120.0
130.0
140.0
150.0
5 PNTS
CURRENT (AMPS) N-200 T-4.0 MS

FIG. 40

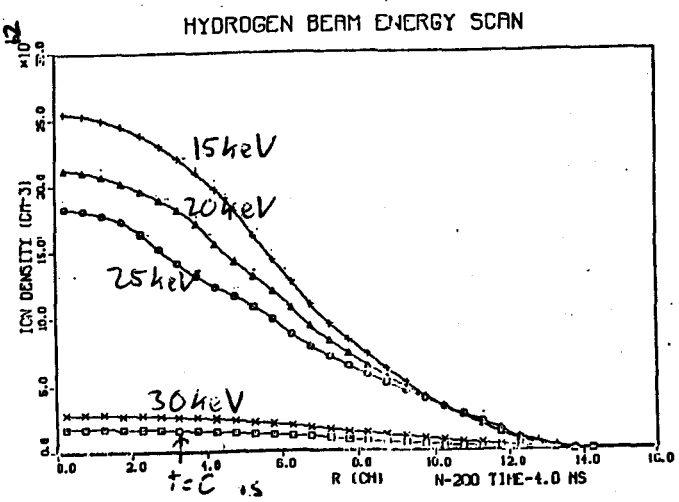

FIG 41

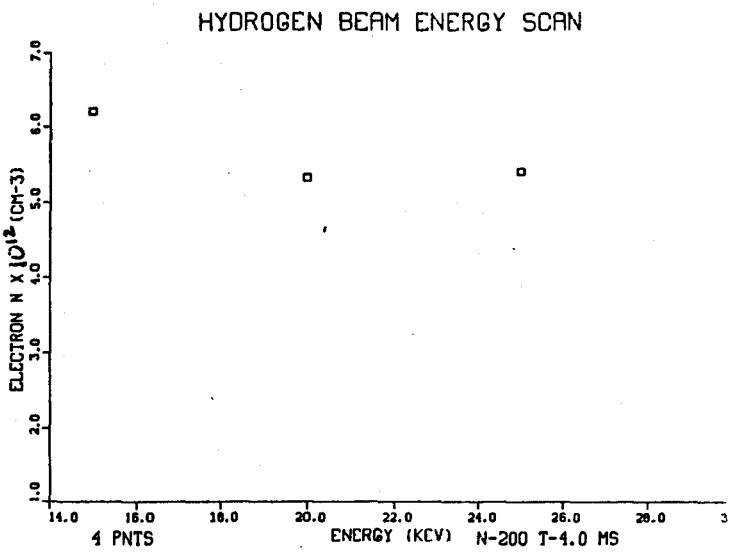

FIG 42

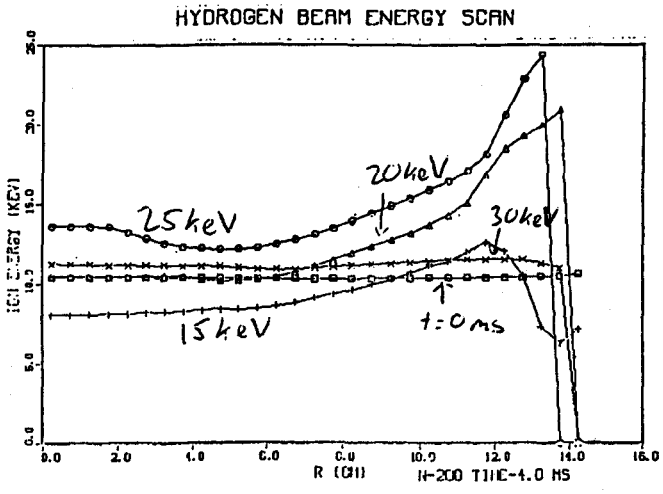

FIG 43

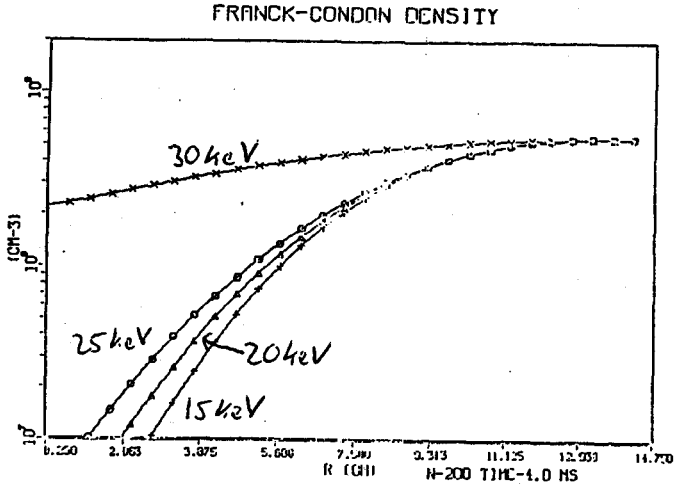

FIG 44

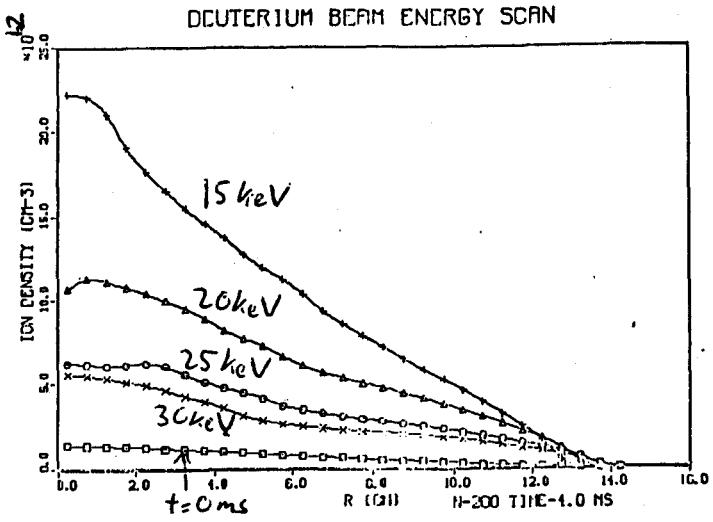

FIG. 45

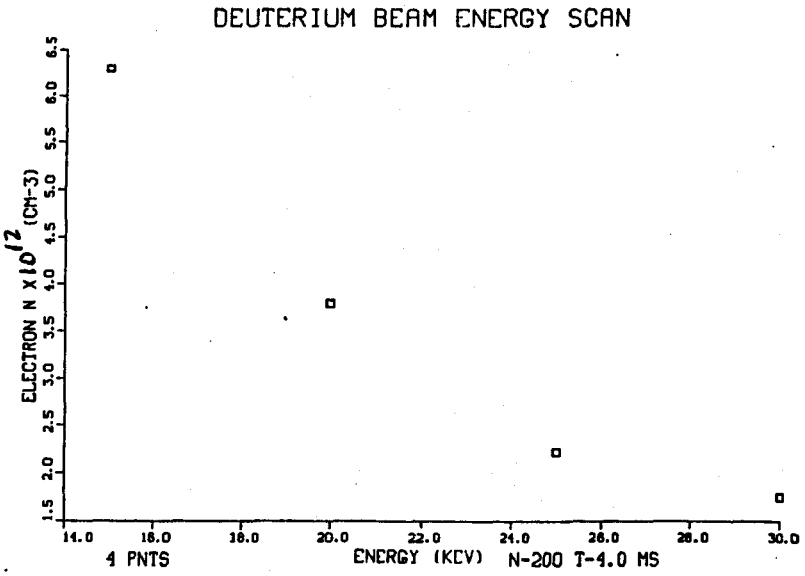

FIG 46

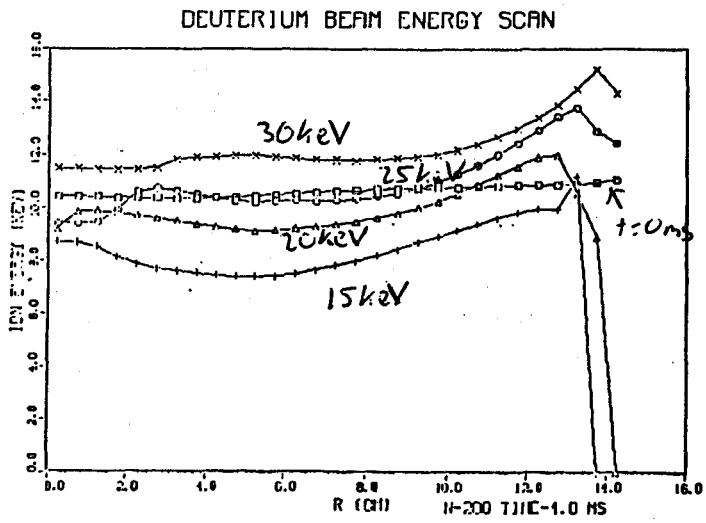

FIG. 47

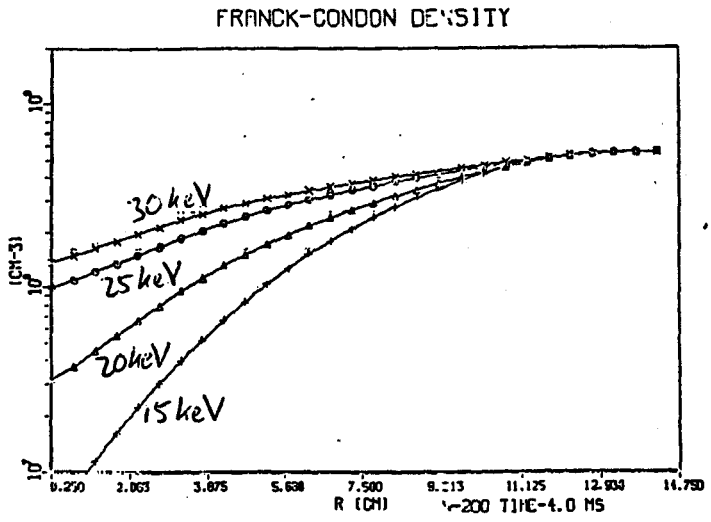
FRANCK-CONDON DENSITY
30 keV
25 keV
20keV
15 keV
R (CM)
N-200 TIME-4.0 MS

FIG. 48

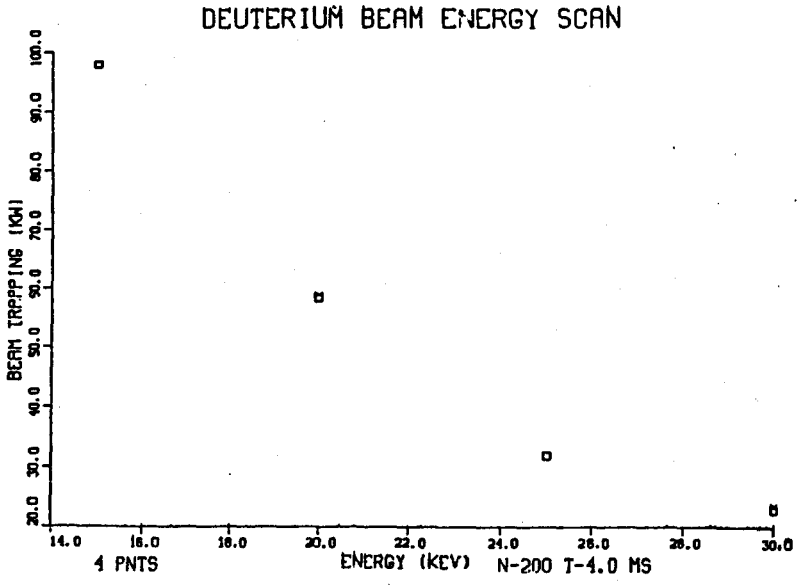
DEUTERIUM BEAM ENERGY SCAN
BEAM TRAPPING (KW)
4 PNTS
ENERGY (KEV)
N-200 T-4.0 MS

FIG. 49

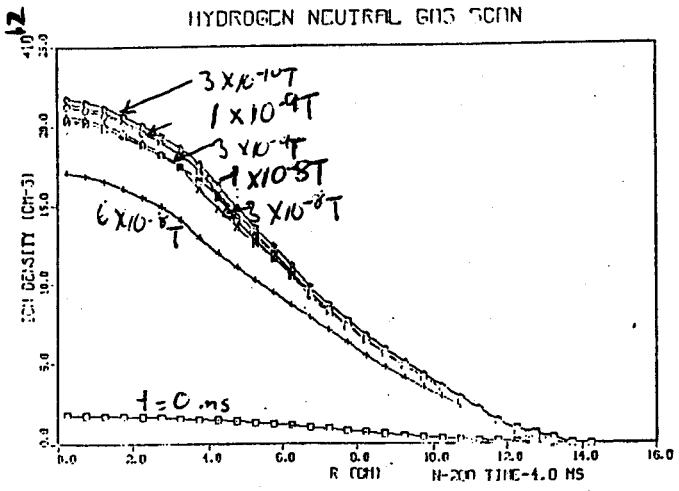

FIG. 50

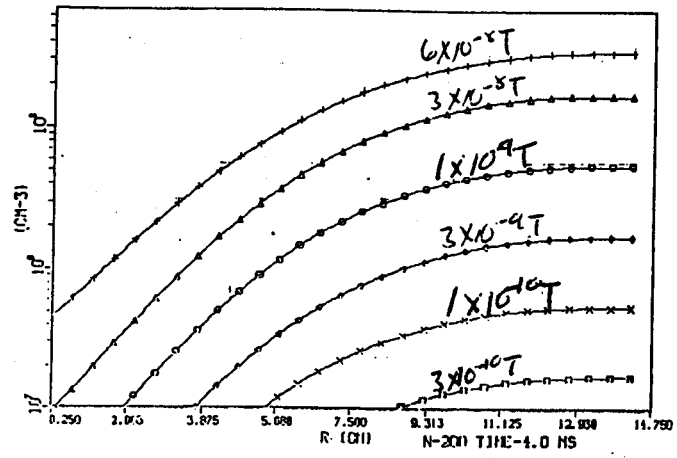

FIG. 51

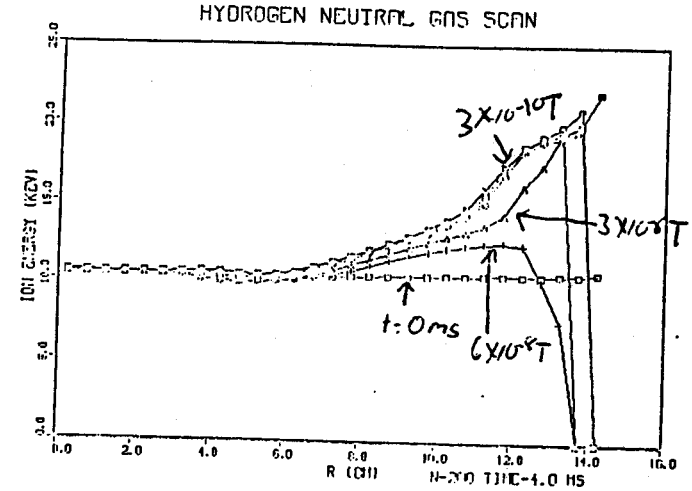

FIG 52

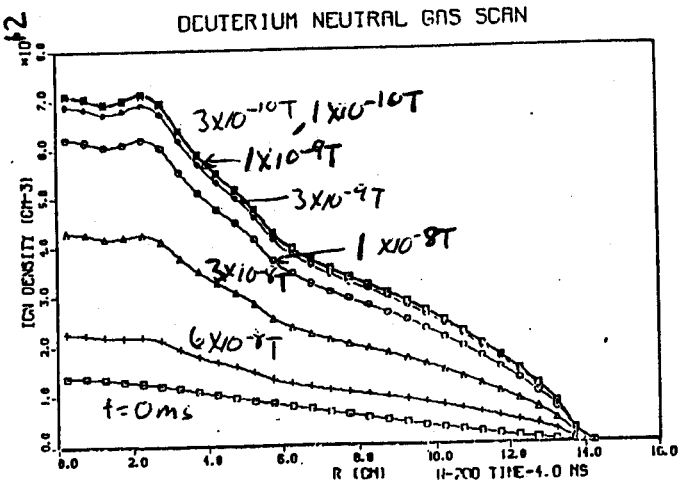

FIG. 53

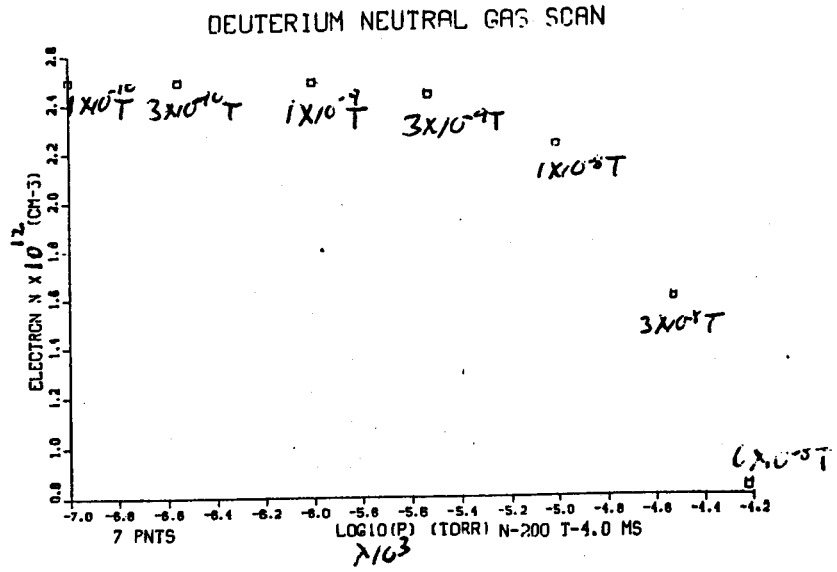

FIG. 54

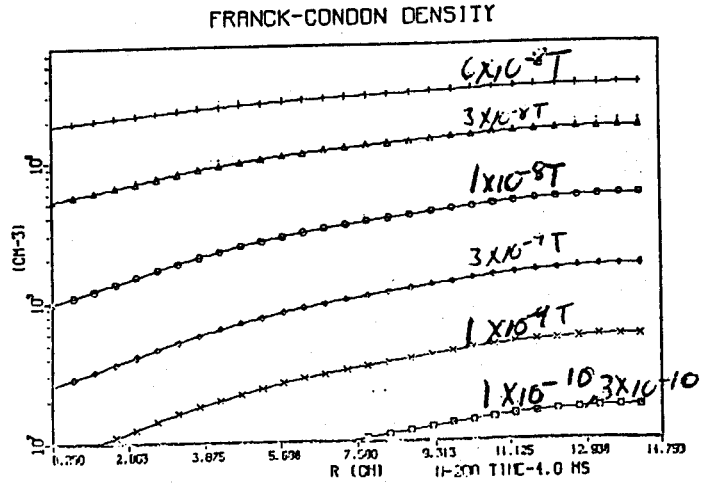

FIG. 55

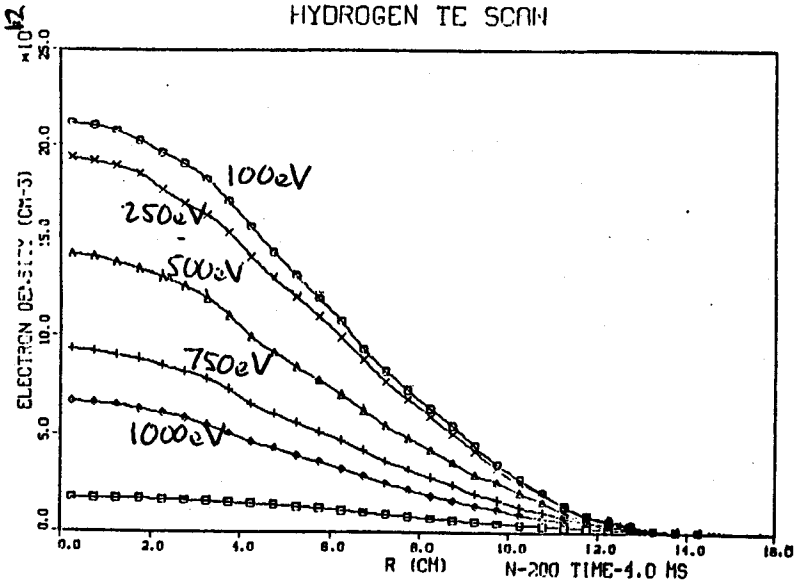

FIG.56

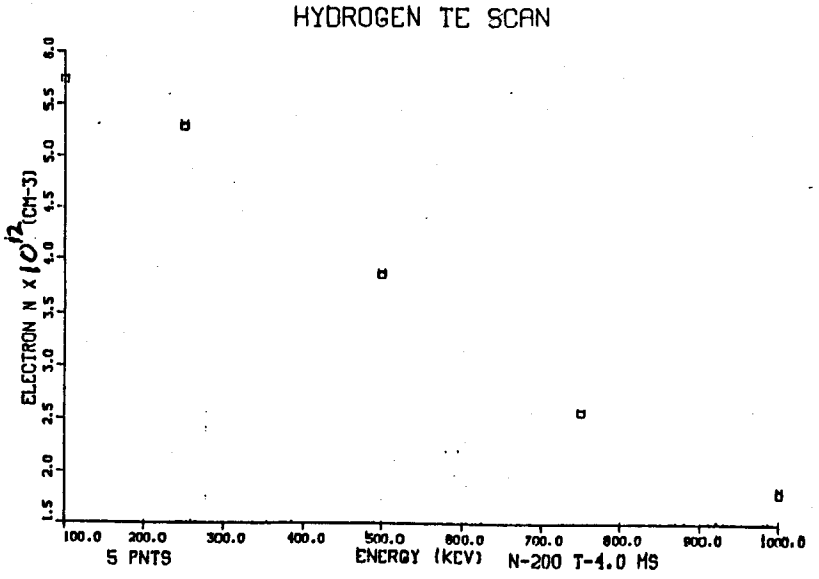

FIG 57

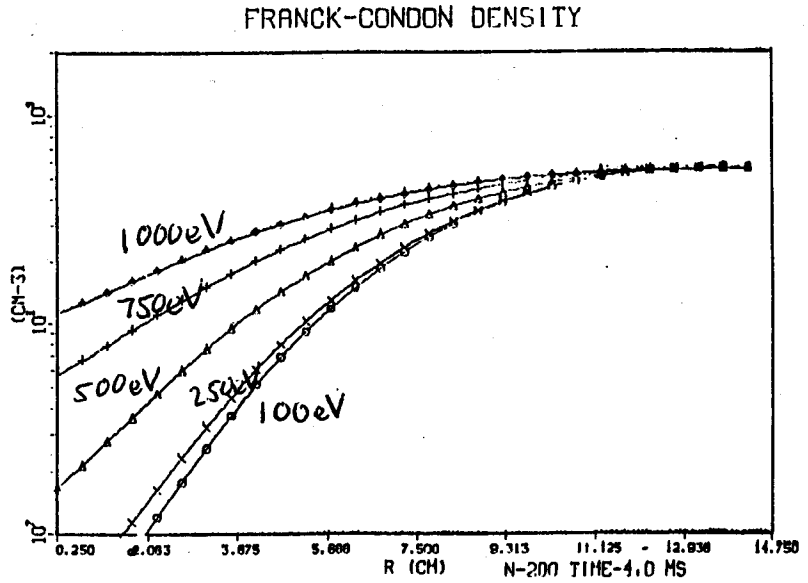

FIG.58

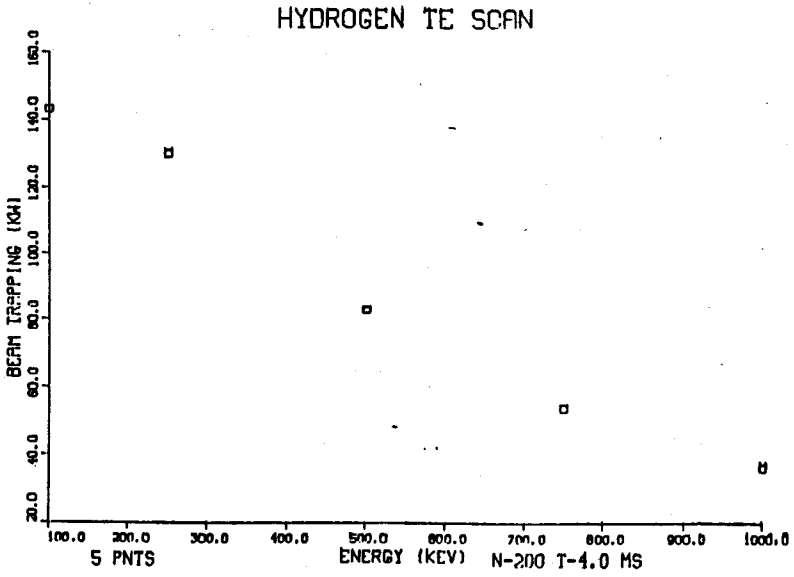

FIG.59

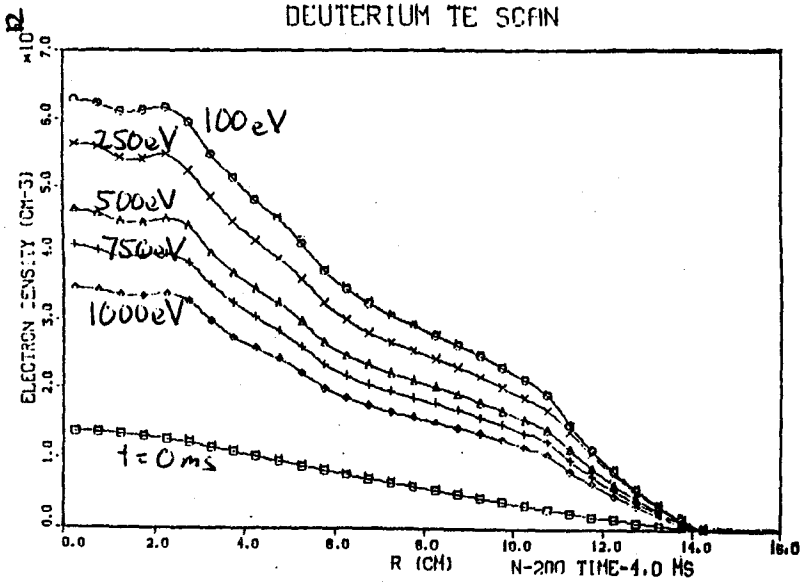

FIG. 60

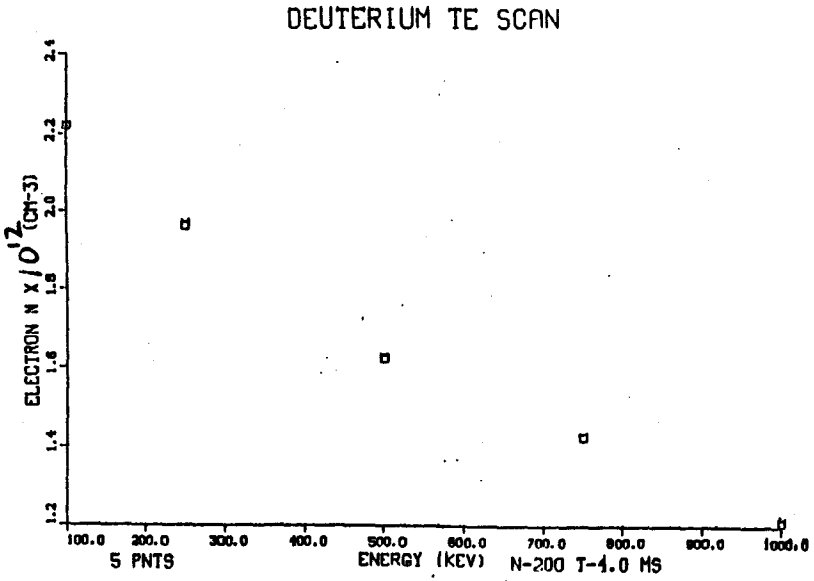

FIG. 61

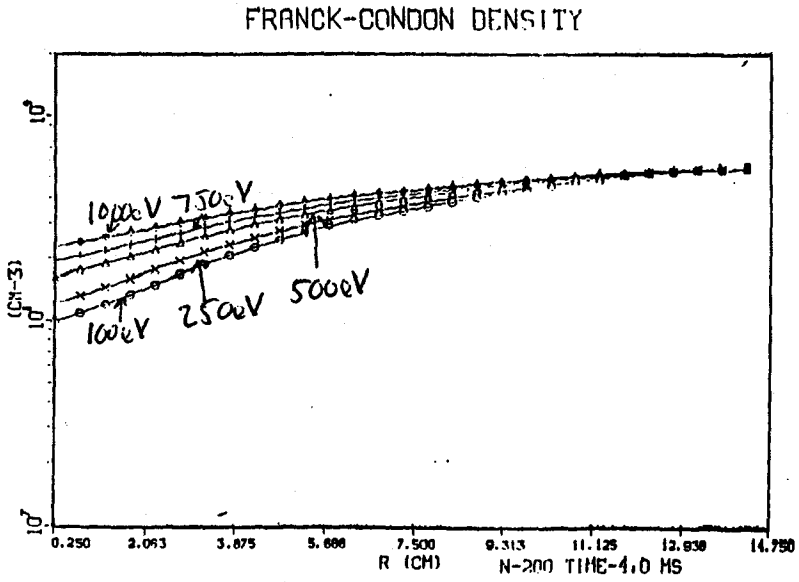

FIG 62

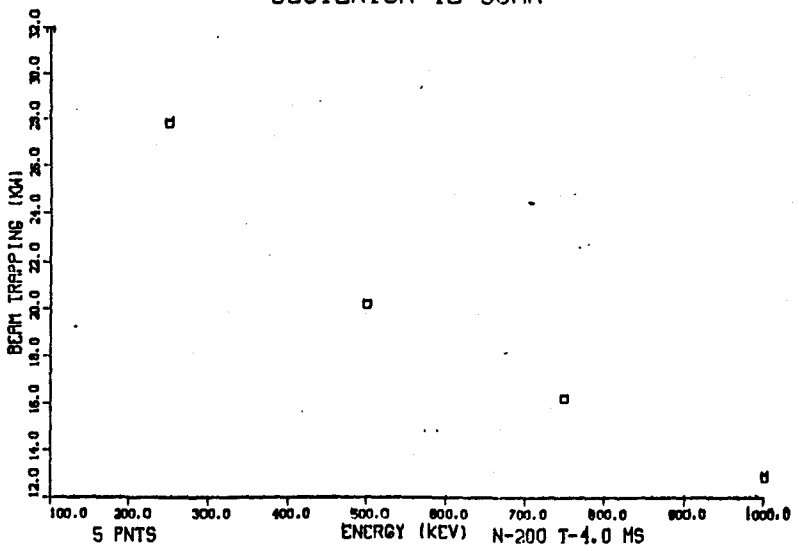

FIG. 63

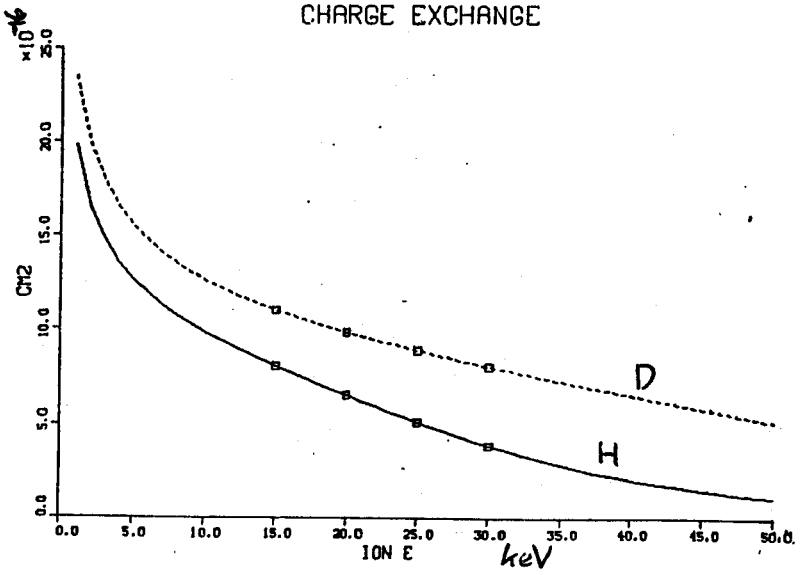
CHARGE EXCHANGE
×10⁻¹⁶
CM2
0.0
5.0
10.0
15.0
20.0
25.0
D
H
0.0
5.0
10.0
15.0
20.0
25.0
30.0
35.0
40.0
45.0
50.0
ION E
keV

FIG. A-1

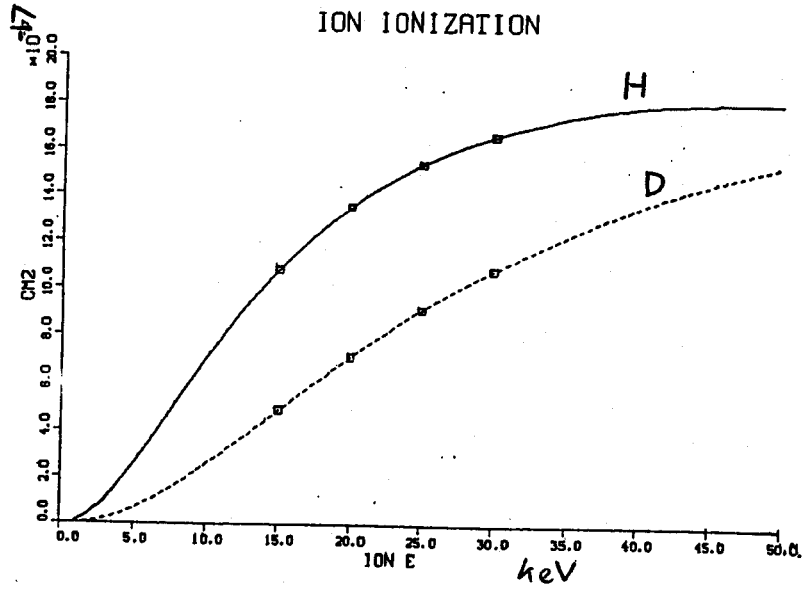
ION IONIZATION
×10⁻¹⁷
CM2
0.0
2.0
4.0
6.0
8.0
10.0
12.0
14.0
16.0
18.0
20.0
H
D
0.0
5.0
10.0
15.0
20.0
25.0
30.0
35.0
40.0
45.0
50.0
ION E
keV

FIG. A-2

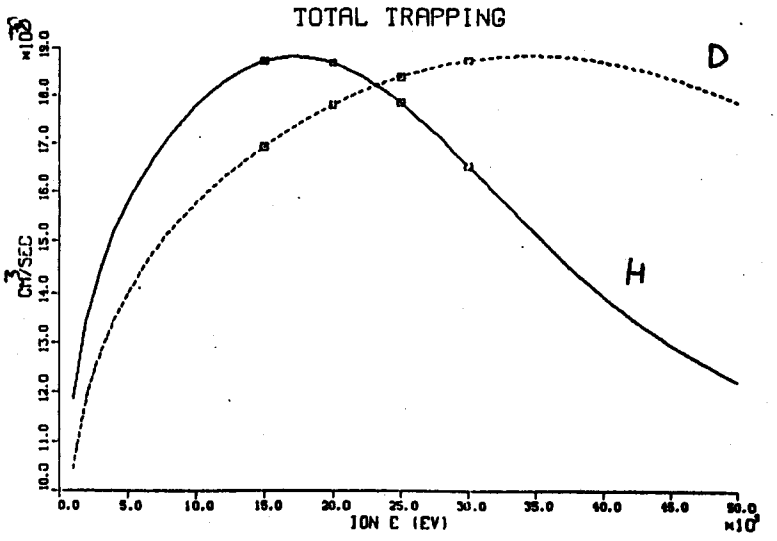

FIG. A-3

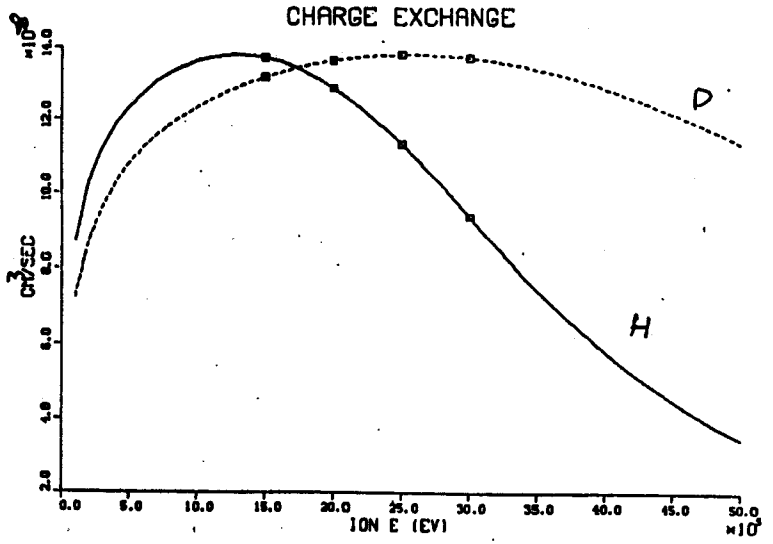

FIG. A-4

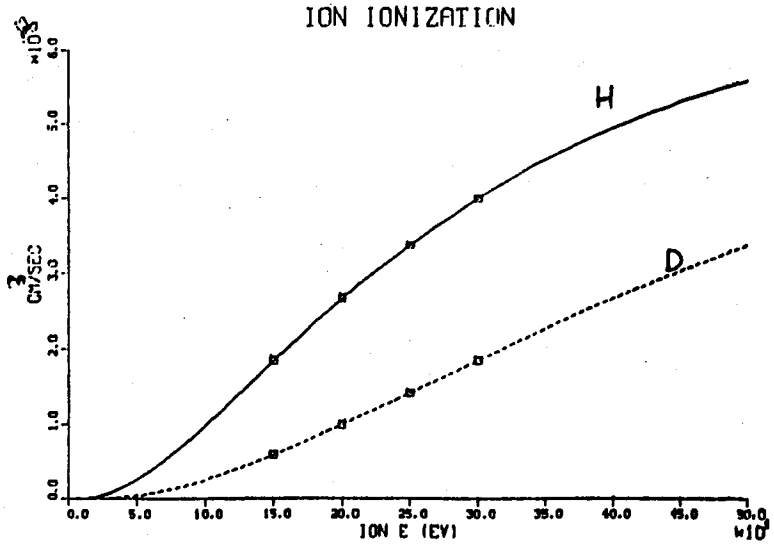

FIG. A-5

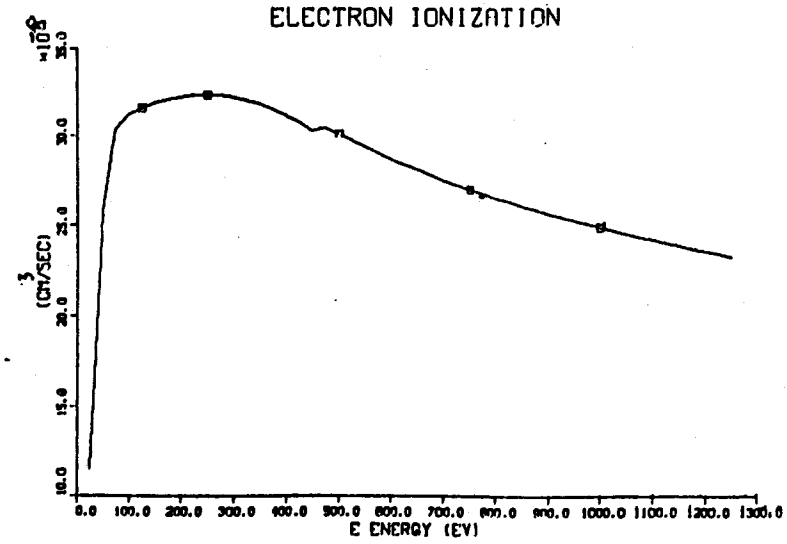

FIG. A-6